PENNSTATE

ARL

NASA GODDARD SPACE FLIGHT CENTER COOPERATIVE ENTERPRISE FINAL REPORT

APPLIED RESEARCH LABORATORY
The Pennsylvania State University
State College, PA 16801
www.arl.psu.edu

6 December 2004

This report was prepared for the NASA Goddard Space Flight Center under Grant # NCC5-508.

Acknowledgments

The Applied Research Laboratory (ARL) team is grateful to the NASA Goddard Research team – Mike Hagopian, Stan Ollendorf, and Ted Swanson – for their sponsorship and guidance in this study. Support from the USAF Air Force Research Laboratory is also gratefully acknowledged.

ARL PROJECT TEAM

JOSEPH E. FREDLEY, *Project Leader, Capillary Heat Pump*
DANIEL B. LYSAK, *Shearography*

Contents

Executive Summary 1

Appendix A: Capillary Heat Pump Final Report 3

Appendix B: Shearography Final Report 34

Executive Summary

This cooperative agreement between the Applied Research Laboratory at the Pennsylvania State University (ARL/PSU) and the Mechanical Systems Center at The NASA Goddard Space Flight Center (NASA/GSFC) provided a means for the NASA/GSFC to utilize the advanced technologies of the ARL/PSU in direct support of NASA/GSFC research and development or flight programs, and afforded the NASA/GSFC the opportunity to test and characterize ARL/PSU technologies to advance their development. This agreement also provided a mechanism for ARL/PSU and NASA/GSFC to conduct preliminary work in advance of teaming when responding to NASA Research Announcements or other Requests for Proposals. Two primary topics of research were pursued during the execution of this agreement: Capillary Heat Pump for spacecraft thermal management, and Shearography for nondestructive inspection.

Numerical analysis was performed to examine the viability of a Capillary Heat Pump (CHP) concept using a Loop Heat Pipe (LHP) evaporator and an eductor in a closed loop to reject heat at a higher temperature than it is acquired at with the goal of reducing a spacecraft's radiator area. The conceptual analysis indicates the eductor inefficiency resulting from the mixing of the high velocity motive flow with the low velocity suction flow may preclude the savings of spacecraft radiator area. The energy required to create motive flow vapor is greater than the additional energy the radiator can reject at the higher radiator temperature condition generated by the eductor. Additionally, the spacecraft's electrical power (e.g., solar array size) would have to increase to supply the energy for creating the eductor motive vapor. The utility of a CHP to spacecraft thermal management may be limited to those missions where system reliability is the most critical design requirement and any mass penalties resulting in the use of the CHP is considered secondary. Application of CHP to Lunar or Martian surface missions, where a heat pump is required to accommodate the relatively high thermal rejection temperatures, may be appealing if energy sources can be easily harnessed to generate the eductor motive vapor. A detailed final report on the CHP study is included as Appendix A.

The applicability of shearography techniques for nondestructive inspection and evaluation was examined in two unique application areas. Shearography is shown to give good results in evaluating the quality of bonds holding lead tiles to the SWIFT spacecraft BAT gamma ray mask. Using a vibration excitation, poorly bonded tiles can be readily distinguished from those that are well bonded. The shearography results were compared to pull tests performed on a set of tile samples. The second application was to evaluate

the bonding between the skin and core of a specular surface honeycomb structure. A novel technique was developed that allows specular objects to be evaluated using shearography. The technique readily identifies large scale bond failures in the panel, although some scaling issues regarding the particulars of the panel need further examination. As a result of this work, NASA discussed with ARL/PSU the possibility of using shearography for inspection of the space shuttle external tank foam panel attachment and for inspection of the space shuttle wing leading edge thermal protection system. NASA has issued a contractor's technical report (CR-2003-212231, December 2003) describing the shearography work performed during this cooperative agreement. A detailed final report on the shearography effort is included as Appendix B.

APPENDIX A

Capillary Heat Pump

Final Report

To: NASA Goddard Space Flight Center
(Grant number NCC5-508)

Submitted by:
Joseph E. Fredley
The Applied Research Laboratory
The Pennsylvania State University
30 November 2004

ABSTRACT

The viability of a Capillary Heat Pump (CHP) concept using a Loop Heat Pipe (LHP) evaporator and an eductor in a closed loop to reject heat at a higher temperature than it is acquired at with the goal of reducing a spacecraft's radiator area is examined. The conceptual analysis undertaken here indicates the eductor inefficiency resulting from the mixing of the high velocity motive flow with the low velocity suction flow may preclude the savings of spacecraft radiator area. The energy required to create motive flow vapor is greater than the additional energy the radiator can reject at the higher radiator temperature condition generated by the eductor. Additionally, the spacecraft's electrical power (e.g., solar array size) would have to increase to supply the energy for creating the eductor motive vapor. The utility of a CHP to spacecraft thermal management may be limited to those missions where system reliability is the most critical design requirement and any mass penalties resulting in the use of the CHP is considered secondary.

INTRODUCTION

The most advanced thermal control systems currently operating in space are based on capillary pumped loop (CPL) (Chalmers (1)) or LHP technology. Both technologies are passive systems using porous media to promote circulation of a working fluid around a closed loop. These systems acquire energy from a source at a temperature that is higher than the sink temperature the energy is rejected to. A typical CPL application used for instrument thermal control would have the evaporator acquiring heat at about 20 °C and rejecting the acquired energy via a radiator at about 0 °C. The radiator would view a thermal sink at a temperature on the order of –220 °C. In comparison, a heat pump system is capable of acquiring energy at 20 °C and rejecting the energy via a radiator at a temperature greater than 0 °C. Raising the radiator temperature would allow greater heat rejection per unit area of radiator. However, for a heat pump to be of benefit, it must have sufficient efficiency such that the additional energy required to motivate the heat pumping is less than the radiator heat rejection capability gained by the resulting increase in radiator temperature. The benefits of using mechanical compressor based heat pumps for spacecraft thermal control is described in detail by Scaringe (2). Whether a heat pump system makes sense for low sink temperature applications depends on mission specifics such as power available, mass budget, available radiator area, etc. For system designs being contemplated in support of the Nuclear Space Initiative, there is a large amount of thermal energy that must be rejected to space. The radiator area required for these applications may be very large. A heat pump system of sufficient efficiency would maximize radiator effectiveness which, for a given acquired heat load, would result in minimum radiator area and mass.

Another scenario exists where a heat pump thermal control system may be the only solution. For missions where the available thermal sink temperature is greater than the thermal source temperature, the only means of effecting thermal control is using a heat pump. For example, calculations supporting thermal control on the lunar surface indicate that the lunar mid-day thermal sink temperature (which is the design driver) would be about 38 °C as reported by Swanson (3). A Mars surface mission may have similar requirements.

Mechanical heat pump systems in the form of Stirling coolers have being flying in space for some time. They are used to achieve very low source temperatures and typically have a lifetime of less than five years. Larger systems for handling more substantial thermal loads at higher source temperatures may be achievable but would likely exhibit the low reliability of their low temperature predecessors and would produce a significant vibration source to deal with. Absorption heat pump systems have been studied but I do not believe they have been flown in space. Extending CPL and LHP technology used in current advanced heat transport systems to support a heat pump system design that would be very reliable and without vibration may be advantageous. The following discussion of an eductor-based capillary heat pump (CHP) system's design addresses this potentiality.

BACKGROUND

Headley (4) reports that eductor (or ejector) based systems were first used before 1901 by LeBlanc of France and by Parsons of England, who are credited with its invention. Figure 1 illustrates a basic eductor heat pump system. A mechanical pump forces liquid into a vapor generator where, with the addition of heat, vapor is created and injected into an eductor as the motive fluid. Liquid exiting a condenser is throttled and directed into an evaporator. The eductor uses the motive fluid from the vapor generator to entrain vapor from the evaporator and generate an eductor exit flow with a pressure greater than that of the evaporator. While the eductor does the vapor compression instead of a mechanical compressor, a liquid pump is still necessary to promote loop circulation. The attraction of this system is that the high cost, high weight, vibration signature, and low reliability of the mechanical compressor is replaced with a light weight, low cost, highly reliable device that produces minimal vibration. Also, thermal energy, instead of electrical energy, can be used as input for the eductor motive fluid allowing for waste heat utilization. As Al-Ansary (5) states, nevertheless, eductor-based systems are not yet nearly as popular as conventional systems because of their significantly lower thermal efficiency. The critical component in limiting system efficiency is the eductor itself.

Figure 2 illustrates a typical eductor. Motive flow enters the eductor at station 0 at a high pressure and temperature and expands to a very high velocity through the converging-diverging eductor inlet nozzle. This high velocity flow exits the nozzle at station 1. Low pressure and low velocity vapor from the evaporator enters the eductor at station 2 and is entrained by the high velocity motive fluid. The combined flow passes through the eductor throat, station 3, and through the diffuser where velocity is exchanged for pressure. The mixture exits the eductor at station x to enter the condenser. As Al-Ansary (5) states, since the motive flow starts the mixing process at a very high velocity while the entrained flow starts at a negligibly small velocity, eductors have an inherent momentum mismatch problem which causes great losses of available energy. This results in low eductor efficiency.

Eductor-based systems have been analyzed for space applications. Nord (6) presents an analysis of a solar powered integrated thermal management and power cycle in a system that combines a thermal management and a power producing cycle into a single system. An eductor provides the compression in the thermal management subsystem. The analysis focussed on determining the minimum combined radiator and solar collector area for a range of system operating conditions. Kandil (7) reports the results of analyzing the Nord (6) system with the addition of a recuperator in the power management subsystem.

CAPILLARY HEAT PUMP (CHP) CONCEPT

Figure 3 illustrates the CHP concept. Essentially, it is the same configuration as shown in Figure 1 except that the liquid pump and vapor generator have been replaced with the compensation chamber and porous media evaporator pump of a LHP. Heat supplied to

the LHP-evaporator generates saturated vapor at significantly higher pressure than the entering liquid. Sintered metal porous media with a pore diameter of 0.5 microns is commercially available for use in a LHP-evaporator. This porous media yields a pressure rise potential across the LHP-evaporator of about 72 psi for water and about 25 psi for methanol. With some development, it may be possible to use 0.25 micron sintered metal porous media in the LHP-evaporator. This would result in double the pressure rise potential of the 0.5 micron porous media.

The high pressure saturated vapor exiting the LHP-evaporator is supplied to the eductor inlet nozzle. The heat rate acquired at the evaporator combined with the heat rate supplied to the LHP-evaporator is rejected at the condenser. The resulting system has no moving parts and is capable of delivering energy to the condenser at a greater temperature than acquired at the evaporator. The challenge is to design a system (system configuration and operation, eductor design, fluid selection) that maximizes the heat rate acquired at the evaporator, minimizes the heat rate supplied to the LHP-evaporator, and maximizes the pressure rise across the eductor. This must be done within the pressure rise capability of the LHP-evaporator for an assumed pore size and working fluid. As discussed earlier, the eductor is the critical system component limiting CHP operational performance. It is crucial that eductor operation be well understood and that ways to improve its efficiency be explored if a CHP system is to be viable for most low sink temperature applications. Optimizing eductor efficiency is essential from the aspect of minimizing radiator area and mass when considering application to high temperature sink missions.

EDUCTOR ANALYSIS

Eductors have been studied theoretically and experimentally by many people. Lu (8) analytically modeled an eductor assuming steady isentropic ideal gas flow and compared his predictions to experimental data. His studies identified optimized ranges for critical eductor parameters defining eductor geometry and nozzle spacing. Al-Ansary (5) used a homogeneous equilibrium model to predict eductor performance independent of specific eductor geometry. He also assumed steady isentropic flow but also concluded there are only minor differences in prediction when assuming ideal gas or using real fluid properties.

The eductor analysis presented here was meant to support eductor design in preparation for experimentation. For this reason, specific eductor geometry is used and motive vapor mass flow rates consistent with a maximum available LHP-evaporator heat rate of 1 kW are assumed. Conservation equations for energy, momentum, and mass flow are developed for sections of the eductor depicted in Figure 2. Speed of sound calculations for the flow is performed using the method developed by Bursik (9) for gas-liquid mixtures. His method calculates the correct sound speeds for saturated liquid and saturated vapor conditions and correctly predicts the reduced sound speeds that occur for two-phase conditions. Rough approximations are made in the modeling to account for flow losses by using the approach indicated by Crane (10) for flow through ducts of

varying cross-sectional area. All equations are solved using the Engineering Equation Solver (EES) developed by Klein (11). The EES software includes fluid property data for most refrigerants. As the equation input to EES is very self-explanatory, the individual equations are not reproduced here but can be viewed in the sample EES input file found in Addendum A.

The eductor inlet nozzle that converts high pressure low velocity vapor into low pressure supersonic vapor is modeled first. The first section addressed is flow from the nozzle inlet, station 0, to the nozzle throat, station t in Figure 2. The second section covers the flow from the nozzle throat to the nozzle exit, station 1. Predictions are made for these two sections initially by gradually lowering the nozzle exit pressure until the throat velocity matches the calculated throat sonic velocity. Once this choked flow condition has been found, the three conservation equations for the first section are disabled and the throat pressure and velocity, and mass flowrate are specified. Further reduction in nozzle exit pressure yields increasing exit velocity.

The third section of input coding models the flow from the evaporator, station e, into the eductor, station 2. The pressure at stations 1 and 2 are assumed to be equal.

The fourth coding section models the flow in the eductor's mixing region from stations 1 and 2 to station 3, the eductor throat. Flow velocity is checked against the calculated sonic velocity at the eductor throat.

The final coding section models flow from the eductor throat to the eductor exit, station x. This is the diffuser where flow velocity is exchanged for pressure.

Independent variables for this analysis include:

x0	motive flow quality at inlet to supersonic nozzle
P0	motive pressure at inlet to supersonic nozzle
D0	supersonic nozzle inlet diameter
Dt	supersonic nozzle throat diameter
theta0	supersonic nozzle convergence angle
D1	supersonic nozzle exit diameter
thetat	supersonic nozzle divergence angle
Pe	evaporator pressure
xe	evaporator quality
De	diameter where evaporator flow enters the eductor
D2	eductor mixing region diameter
D3	eductor throat diameter
theta2	eductor mixing region convergence angle
P3	eductor throat pressure
Dx	eductor exit diameter
theta3	eductor diffuser angle

Dependent variables for which the code calculates values include:

Px	eductor exit pressure
mdotm	motive mass flow rate
mdote	evaporator mass flow rate
mdotc	mass flow rate provided to the condenser
ER	entrainment ratio (evaporator vapor mass flow divided by motive vapor mass flow rate)
P,h,T,x,s	pressure, enthalpy, temperature, quality, and entropy at the various eductor stations modeled

ANALYTICAL RESULTS

Tables 1 and 2 summarize the analytical modeling results using water and methanol, respectively. In all cases, the eductor throat pressure, P3, has been selected such that the resulting eductor throat velocity is sonic.

The first set of figures present results of eductor performance using water as the working fluid. The eductor inlet nozzle has been sized to provide a saturated vapor mass flow consistent with a heat input to the LHP-evaporator of about 700 Watts assuming a pressure of 50 psia. This eductor inlet nozzle geometry is used throughout the predictions made using water. As a result, the motive vapor mass flow rate varies for the analyses performed. Figures 4 and 5 were created assuming an eductor inlet nozzle inlet pressure of 50 psia and an evaporator pressure of 0.4 psia. Figure 4 illustrates the effect varying the eductor throat diameter, D3, has on the eductor exit pressure, Px. As one would expect, the eductor exit pressure decreases with increasing eductor throat diameter. Figure 5 shows how the evaporator mass flow rate and the entrainment ratio both increase with increasing eductor throat diameter. Together, these two figures indicate the tradeoff of eductor exit pressure with evaporator mass flow. To get an increase in eductor exit pressure, there is an accompanying decrease in mass flow from the evaporator.

Assuming an eductor inlet nozzle inlet pressure, P0, of 50 psia, and an eductor throat diameter, D3, of 0.22 inches, Figures 6 and 7 indicate how eductor performance varies as a function of the evaporator pressure, Pe. Figure 6 illustrates the eductor exit pressure increasing with increasing evaporator pressure. Figure 7 shows the evaporator mass flow and entrainment ratio increasing with increasing evaporator pressure. Again, this is what one would expect since the evaporator vapor density increases with pressure allowing more mass flow at the same velocity. The increased evaporator mass flow means more momentum for conversion into pressure.

Assuming an evaporator pressure, Pe, of 0.4 psia, and an eductor throat diameter, D3, of 0.22 inches, Figures 8 and 9 indicate how eductor performance varies as a function of the eductor inlet nozzle inlet pressure, P0. Figure 8 illustrates the eductor exit pressure increasing with increasing eductor inlet nozzle inlet pressure. Figure 9 shows the evaporator mass flow and entrainment ratio decreasing with increasing evaporator pressure. One expects the eductor exit pressure to increase as the motive pressure is

increased since more motive mass flow is entering the eductor at about the same velocity, resulting in more momentum for conversion to pressure. The reduction in evaporator mass flow is due to the increased motive flow occupying more of the available eductor throat area, resulting in less flow area available for the evaporator vapor flow.

Assuming an evaporator pressure, Pe, of 0.4 psia, an eductor throat diameter, D3, of 0.22 inches, and an eductor inlet nozzle inlet pressure of 50 psia, Figure 10 indicates how the predicted evaporator mass flow and entrainment ratio vary as a function of the eductor inlet nozzle inlet flow quality, x0. The evaporator mass flow decreases as the eductor motive flow quality decreases. As the motive flow quality is reduced away from a saturated vapor state, the entrainment ratio increases but then decreases at motive flow qualities less than about 0.5. Eductor exit pressure is not affected by the changing motive flow quality.

Figures 11 through 16 indicate the predicted performance for an eductor using methanol as the working fluid. The eductor inlet nozzle has been sized to provide a saturated vapor mass flow consistent with a heat input to the LHP-evaporator of about 700 Watts assuming a pressure of 20 psia. Figures 11 through 16 share the same performance trends as their companion figures, Figures 4 through 9, for water. Figure 17 indicates how the predicted evaporator mass flow and entrainment ratio vary as function of the eductor inlet nozzle inlet flow quality, x0, assuming an evaporator pressure, Pe, of 1.9 psia, an eductor throat diameter, D3, of 0.22 inches, and an eductor inlet nozzle inlet pressure of 20 psia. The evaporator mass flow decreases, and the entrainment ratio increases with decreasing motive flow quality. As with water, eductor exit pressure is not affected by the changing motive flow quality.

While these plots are instructive in describing tendencies and dependencies, it is worthwhile to review the general performance of the water and methanol based eductor analytical predictions in light of potentially replacing a thermal control system like a CPL. Recall from the introduction a typical CPL application where the radiator is at 0 °C. Recall that, for a heat pump system to be of benefit, it must have sufficient efficiency such that the additional energy required to motivate the heat pumping is less than the radiator heat rejection capability gained by the resulting increase in radiator temperature. This can be expressed as ratio of the acquired evaporator heat rate to the supplied LHP-evaporator heat rate, or QR, for the CHP system described. For equal radiator area, the following relates the ratio of radiator heat rejection capability to the ratio of radiator temperatures:

$$\frac{\dot{Q}_2}{\dot{Q}_1} = \left(\frac{T_{abs2}}{T_{abs1}} \right)^4$$

For an equal radiator area solution, QR can be expressed as,

$$QR = \frac{\dot{Q}_{evap}}{\dot{Q}_{LHP}} = \frac{1}{\frac{\dot{Q}_2}{\dot{Q}_1} - 1}$$

Assuming 0 °C as the state 1 radiator temperature, Figure 18 illustrates the relationship of QR to a state 2 radiator temperatures. The curve defines the QR that results in equal radiator area as in state 1. That is to say, for the CHP system, given a heat rate supplied to the LHP, the eductor efficiency is sufficient to raise the radiator temperature enough to just offset the additional radiator area required to handle the supplied LHP heat load. Any eductor QR performance above this curve would yield reduced radiator area.

Comparing the analytical results obtained for water and methanol against Figure 18 is interesting. The predicted ER values have very nearly the same meaning as the QR of Figure 18. The ER values are conservative by 10 to 15 % due to the heat of vaporization being less at the higher motive fluid pressures than at the low evaporator pressures. The ER values, therefore, are a reasonable approximation of the QR. The saturation temperatures consistent with the predicted eductor exit pressures range from 40 °C to as high as 70 °C for water, and range from 30 °C to as high as about 50 °C for methanol. Unfortunately, when a consistent set of eductor exit pressure and ER predictions are used, there are few instances where the QR curve in Figure 18 is reached. Although the eductor design has not been optimized here to try to obtain the necessary QR performance, it does indicate a need to squeeze as much efficiency as possible from the eductor.

DISCUSSION

Croll-Reynolds Company (12) presents an excellent summary of conventional eductor performance for critical designs, that is, designs having sonic velocity at the throat. Croll-Reynolds Company is a major supplier of industrial ejector/eductors. Table 3 summarizes this information. In critical design eductors, it is possible to decrease the motivating pressure without a resulting change in the evaporator pressure if the eductor exit pressure is also decreased. The relation of a change between the motivating pressure and discharge pressure depends on the characteristics of the eductor design. Since an eductor is a one point design unit, once a unit is designed and built to definite specifications of motivating pressure, eductor exit pressure and evaporator pressure, its evaporator suction capacity cannot be increased without changing the internal physical dimensions of the unit. The evaporator capacity is actually lowered by increasing the motivating pressure. Since the eductor inlet nozzle is a fixed orifice metering device, any change in the motivating pressure is accompanied by a proportionate change in the quantity of motive fluid. The Croll-Reynolds summary also warns against using motivating fluid having a quality less than one stating that reduced evaporator suction capability is likely to occur.

Given the goal of increasing the radiator temperature as much as possible, achieving the maximum eductor temperature rise means operating at the low end of a fluid's vapor pressure curve where the dT/dP is the greatest. Low evaporator pressure means low eductor throat pressure which means low throat fluid density. Low density means that in order to get significant mass flow from the evaporator and through the eductor, the eductor throat must be relatively large. Unfortunately, a large eductor throat diameter limits the ability to effect pressure rise (hence temperature rise) across the eductor.

Alternate eductor designs were examined early in the effort reported here. One concept considered a gas/liquid motive flow where liquid present in the motive flow is evaporated as it passes through the eductor. The study hoped to examine ways of converting a heat rate applied to the eductor to pressure rise by making use of the tremendous volume change occurring during evaporation. Bellan (13) and Silverding (14) provide excellent background material for modeling droplet formation and evaporation in two-phase flows. A CFD model, using FLOW3D (15), was developed and simulations were attempted to characterize this approach. Unfortunately, persistent mass conservation problems were encountered with the execution and the modeling effort was suspended.

Efficiency for conventional eductors is usually dominated by the loss of available energy in the eductor's mixing zone where the high velocity motive flow entrains the relatively slow evaporator suction flow. The mixing process of the motive flow and the evaporator suction flow occurs in a violent and rapid manner, and is accompanied with the strong negative impact of large eddies. The process is similar to a free jet issued from the exit of the nozzle that entrains the ambient fluid (evaporator suction fluid) with it. As illustrated in Figure 19, Mark's Handbook (16), it may be more efficient to "pull" on the evaporator flow instead of "pushing" it like in conventional eductors. Figure 19 shows a motive nozzle that is segmented to allow progressive entry of evaporator flow. Cao (17) took this a step further proposing a new eductor design employing a porous conical wall, shown in Figure 20. Cao modeled a similar design with a CFD code assuming incompressible flow. He chose incompressible flow to avoid the difficulties associated with the complexity of eductor structures and multiple turbulent flow streams. Cao's results indicate a significant improvement in eductor efficiency compared to conventional designs.

Another approach considered for increasing eductor efficiency is to use a pair of immiscible fluids where the evaporator fluid has a relatively high heat of vaporization and low molecular weight and the motive fluid has a relatively low heat of vaporization and high molecular weight. This approach is presented by MacCracken (18). MacCracken's design suggests separation of the two liquids exiting the condenser by taking advantage of gravity and the different fluid densities. Separation could be promoted by fluid motion creating centripetal forces where gravity is absent.

Several promising methods for increasing eductor efficiency have been identified. These methods need to be studied more closely to determine which approach, or combination of approaches, would best improve efficiency. Extensions of these methods should also be

considered. For example, instead of progressively "pulling" on the evaporator vapor as suggested by Cao (17), maybe progressively "pushing" on the evaporator vapor by sequentially injecting motive flow yields better performance. Maybe a combination of progressive mixing with gas/liquid motive fluid using a heated eductor will work best. These potential solutions need to be identified and experimentally verified.

RECOMMENDATIONS FOR FUTURE STUDY

Testing of a conventional eductor should be conducted to establish a performance baseline in preparation for exploring improved eductor designs. An eductor has been purchased for use in these baseline tests. The eductor performance quoted by the supplier, Fox Valve (19), is

Motive: 3 lbm/hr of saturated water vapor at 40 psia
Suction: 0.5 lbm/hr of saturated water vapor at 0.6 psia
Discharge: 3.6 psia (max)

Performance information was obtained from a second eductor supplier, Elmridge Inc. (20) that was essentially identical to the Fox Valve unit. The Fox Valve unit was purchased because it was significantly less expensive. Baseline testing should first replicate these quoted conditions and measure eductor performance. Baseline testing should also include exploring the effects of gas/liquid motive flow and, in addition to using water, should use methanol as a working fluid.

Methods for improving eductor efficiency should be examined. Eductor design concepts should be developed that embrace methods for improving efficiency. These design concepts should then be fabricated and tested to measure performance improvement. Detailed analytical modeling should be set aside, for the time being, in favor of obtaining test results. Once a promising design concept(s) has been test verified, detailed analysis should be performed to first understand the performance and then update the design for optimized performance.

ACKNOWLEDGEMENTS

This work was performed as part of a Cooperative Agreement with NASA Goddard Space Flight Center, grant number NCC5-508. Support from the USAF Air Force Research Laboratory is also gratefully acknowledged.

REFERENCES

1 D. Chalmers, J. Fredley and M. Kurtz, "A New Era of Instrument Thermal Management", IAF-00-U.4.03, 51st International Astronautical Congress, Rio de Janeiro, Brazil, October 2 – 6, 2000.

2 R. P. Scaringe and W. Haskin, "Spacecraft Heat Pump Thermal Bus Development Status and Technical Issues", Proceedings of 25th International Energy Conversion Engineering Conference, Vol. 2, August 12, 1990.
3 T. Swanson, et al, "Low-Temperature Thermal Control for a Lunar Base", SAE901242, July 1990.
4 F. A. Headley, Jr.., "Performance Limitations of an Ejector Heat Pump", Masters Thesis, Georgia Institute of Technology, March 1991.
5 H. A. M. Al-Ansary and S. M. Jeter, "Development of a Simple Homogeneous Flow Model of a Two-Phase Ejector", SAE 1999-01-2698.
6 J. W. Nord, W. E. Lear, and S. A. Sherif, "Analysis of Heat-Driven Jet-Pumped Cooling System for Space Thermal Management", Journal of Propulsion and Power, Vol. 17, No. 3, May-June 2001.
7 S. M. Kandil, W. E. Lear, and S. A. Sherif, "Mass Advantages in a Jet-Pumped Active Thermal Management System", SAE 2002-01-3200
8 L. T. Lu and J. C. Champoussin, "Theoretical and Experimental Study of Jet-Pump Cooling Systems", Proceedings of 25th International Energy Conversion Engineering Conference, Vol. 2, August 12, 1990.
9 J. W. Bursik and R. M. Hall, "Metastable Sound Speed in Gas-Liquid Mixtures", NASA TM 78810, March 1979.
10 Flow of Fluids, Crane Company, Technical Paper No. 410, 1978.
11 S. A. Klein, Engineering Equation Solver (EES), University of Wisconsin.
12 Croll-Reynolds Company, "Ejectors and Ejector Theory", Website:www.croll.com/pr/vetheroy.asp
13 J. Bellan, R. S. Miller, and K. G. Harstad, "Evaluation of Droplet-Evaporation Models for Gas-Liquid Flow", NASA Tech Brief, Vol. 22, No. 2, Item #140, February 1998.
14 C. H. Silverding, "Two-Phase Flows with Phase Transition", Lecture Series 1995-06, von Karman Institute for Fluid Dynamics, May 29 – June 1, 1995.
15 AEA Industrial Technology, "HARWELL-FLOW3D, Release 2.3", Harwell Laboratory, May 1990.
16 Mark's Mechanical Engineering Handbook, pg. 1832, 1951.
17 Y. Cao and J. Ling, "Performance Evaluation and CFD Analysis of a New Jet Ejector Employing a Conical Porous Duct", Proceedings of ASME 2001 Fluids Engineering Division Summer Meeting, New Orleans, Louisiana, May 29 – June 1, 2001, FEDSM2001-18153.
18 C. D. MacCracken, "Immiscible Propellant and Refrigerant Pairs for Ejector-Type Refrigeration Systems", U.S. Patent, No. 4,761,970, August 9, 1988.
19 Fox Valve Development Corporation, December 3, 2002.
20 Elmridge Incorporated, December 3, 2002.

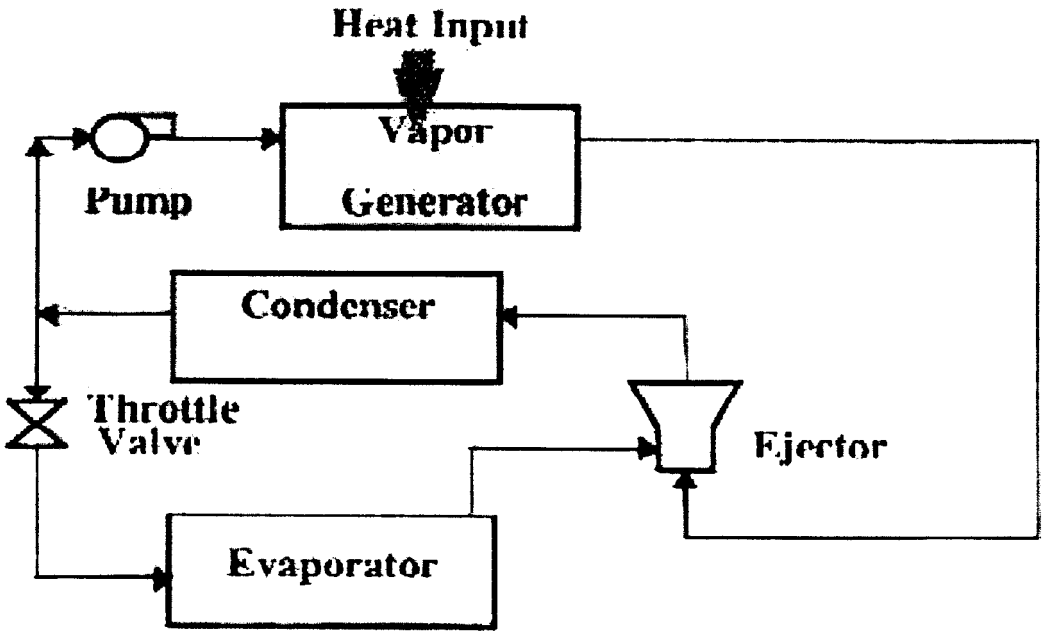

Figure 1. Basic Eductor Heat Pump System

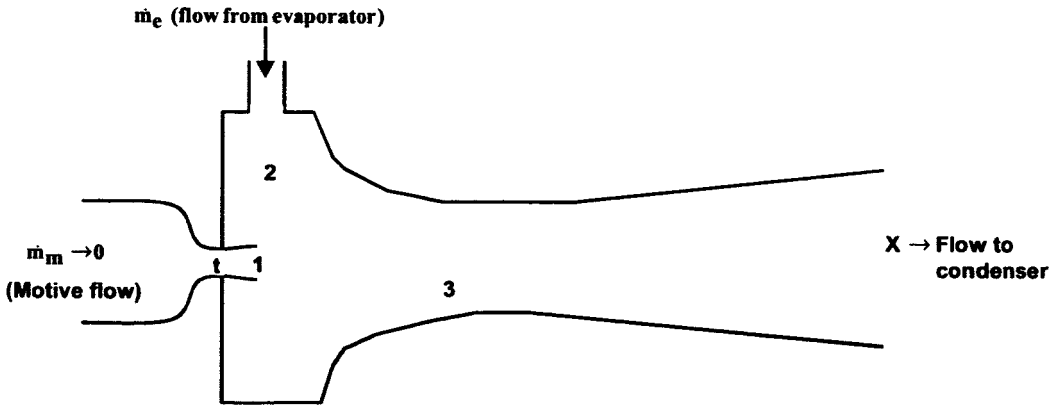

Figure 2. Typical Eductor

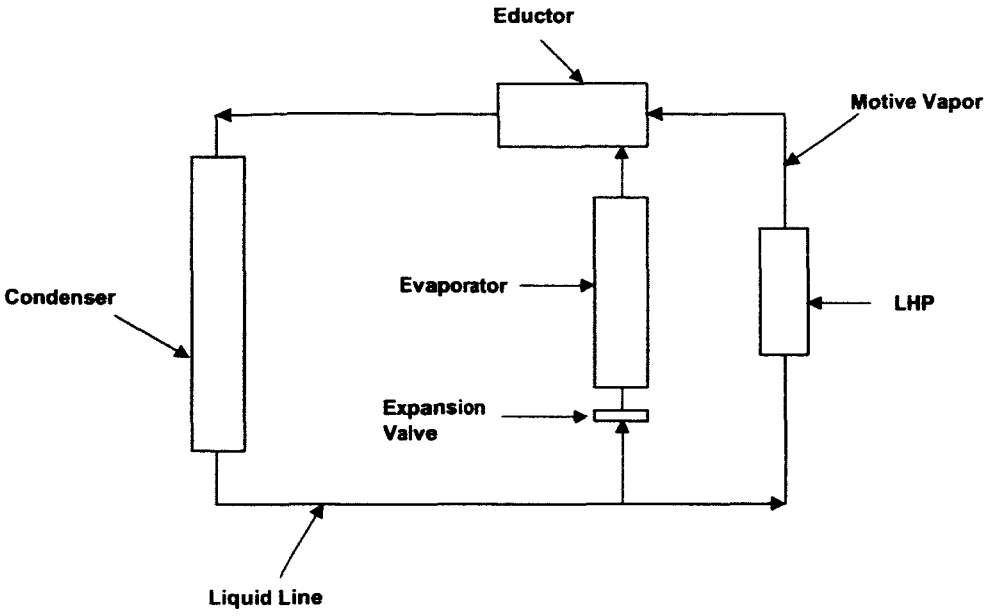

Figure 3. CHP Concept

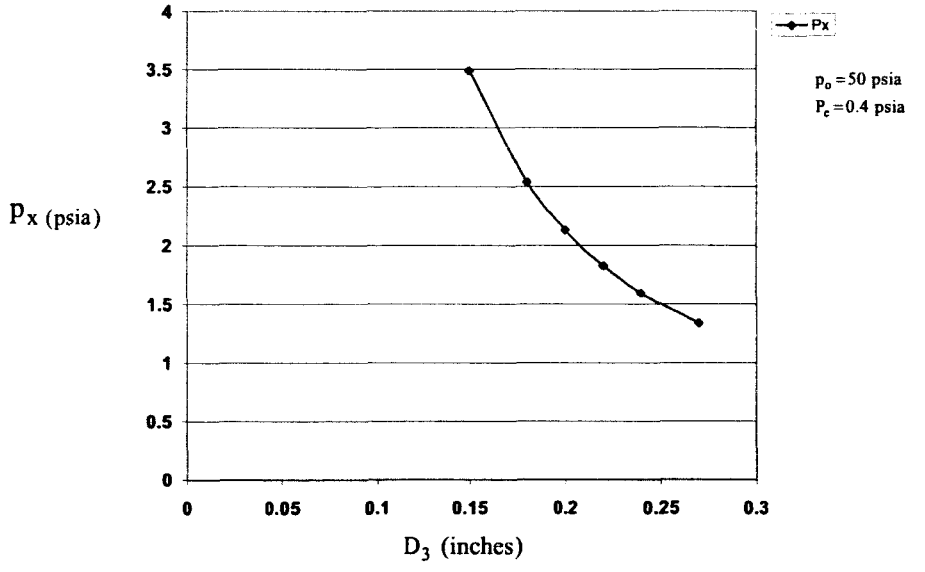

Figure 4. Eductor Exit Pressure Sensitivity to Eductor Throat Diameter for Water

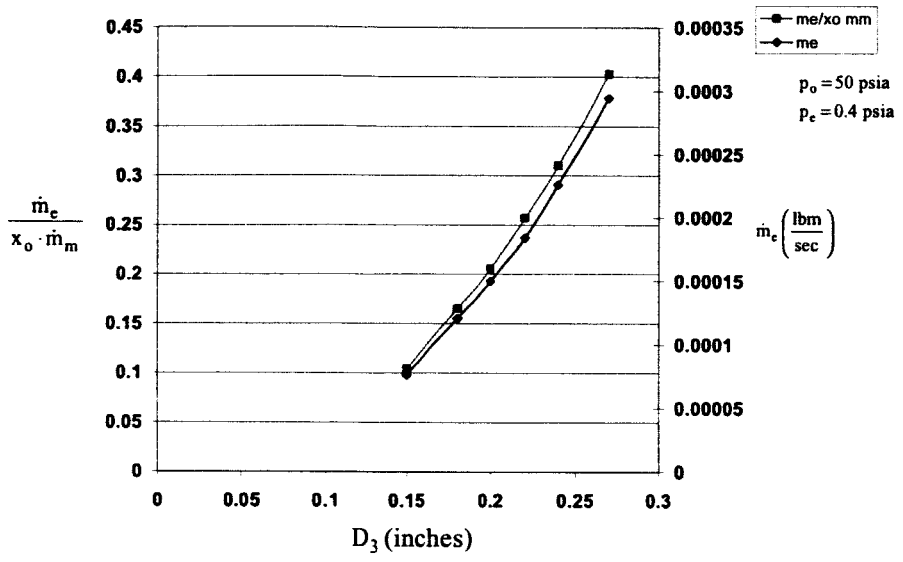

Figure 5. Eductor Evaporator Mass Flow and Entrainment Ratio Sensitivity to Eductor Throat Diameter for Water

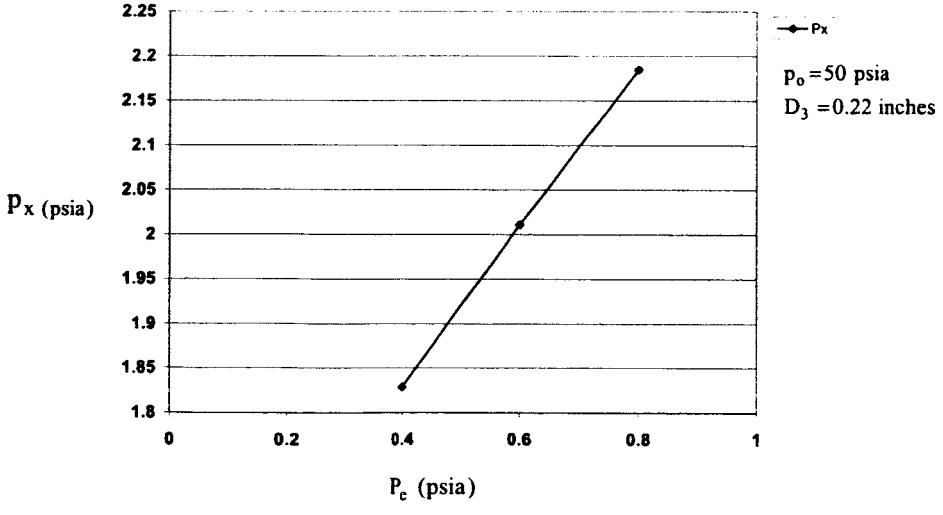

Figure 6. Eductor Exit Pressure Sensitivity to Evaporator Pressure for Water

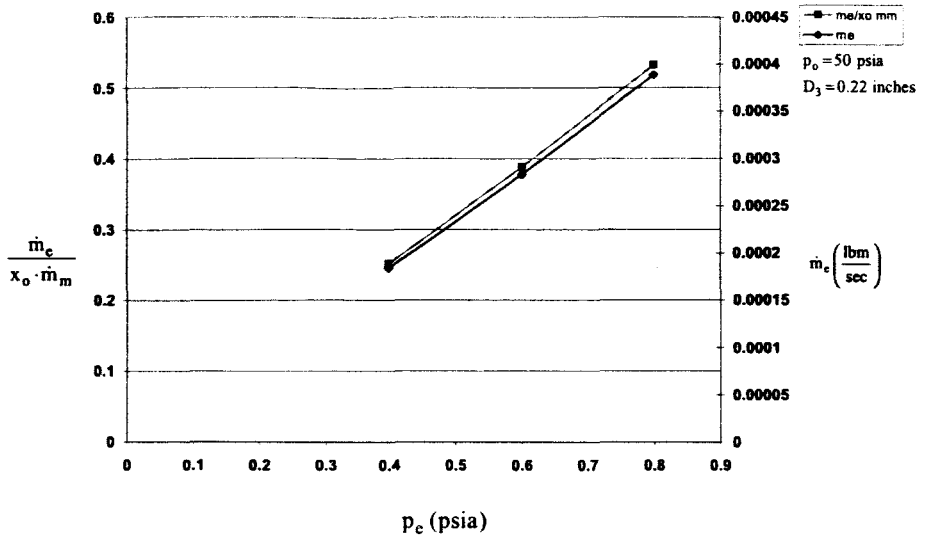

Figure 7. Eductor Evaporator Mass Flow and Entrainment Ratio Sensitivity to Evaporator Pressure For Water

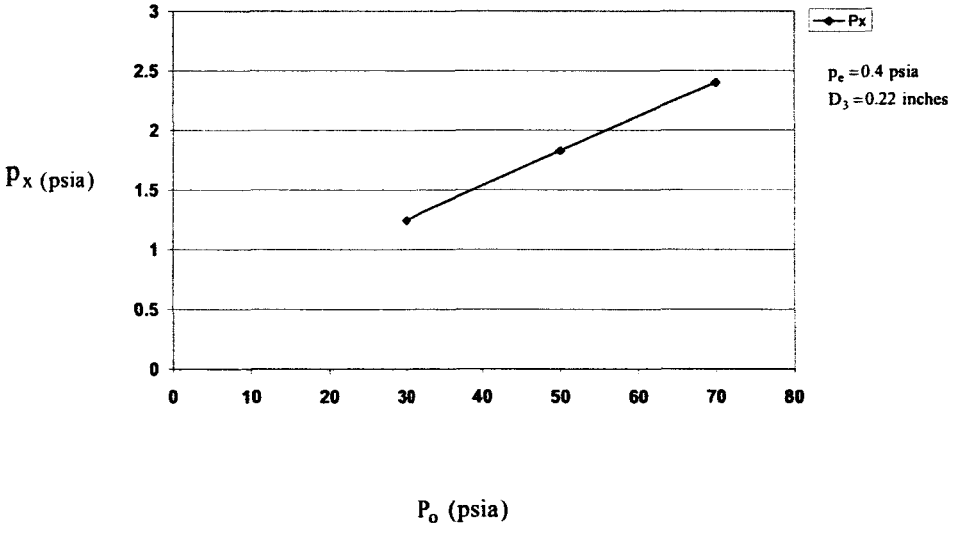

Figure 8. Eductor Exit Pressure Sensitivity to Motive Pressure for Water

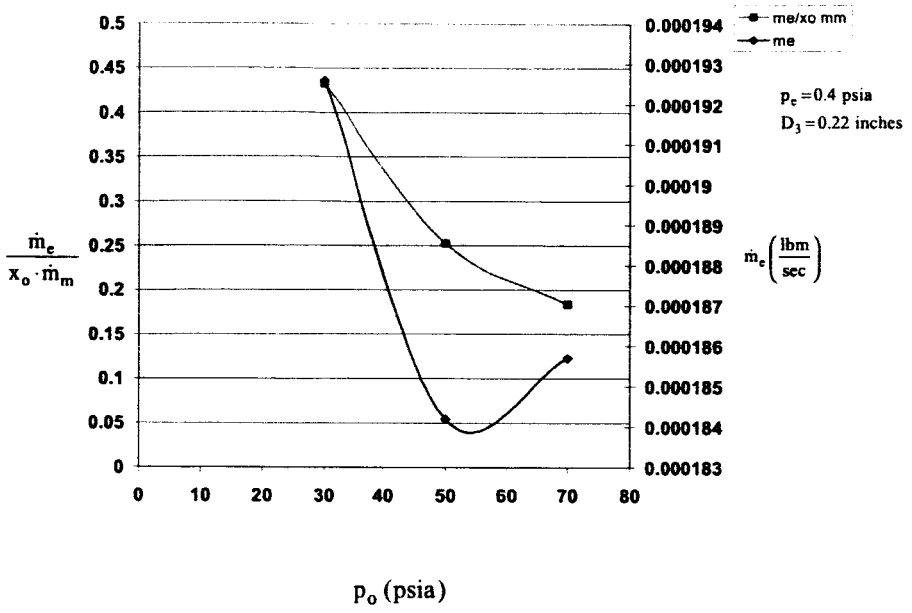

Figure 9. Eductor Evaporator Mass Flow and Entrainment Ratio Sensitivity to Motive Pressure for Water

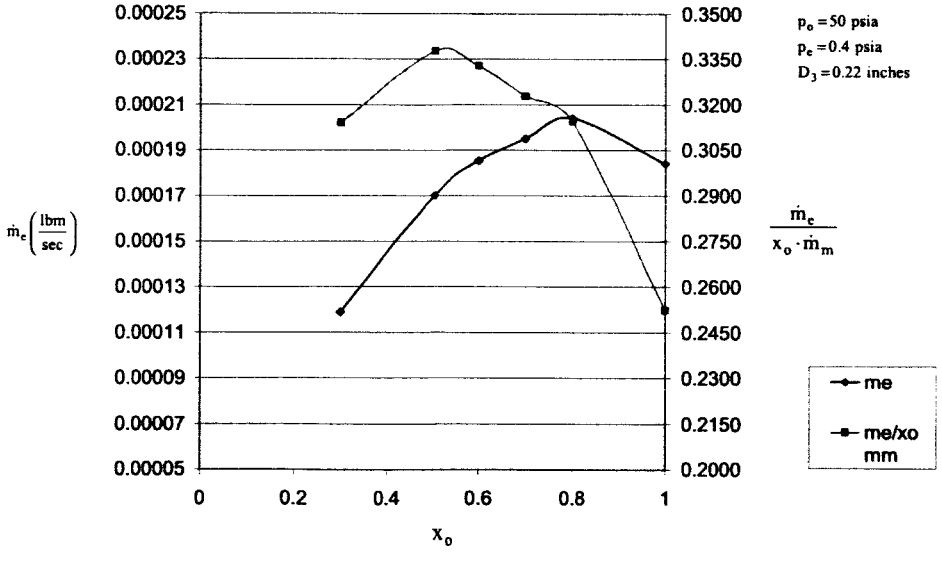

Figure 10. Eductor Evaporator Mass Flow and Entrainment Ratio Sensitivity to Motive Flow Quality for Water

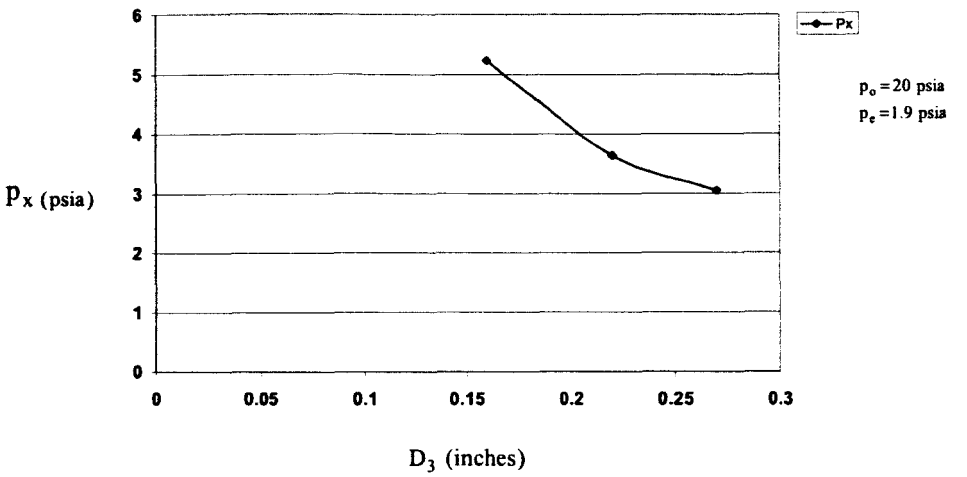

Figure 11. Eductor Exit Pressure Sensitivity to Eductor Throat Diameter for Methanol

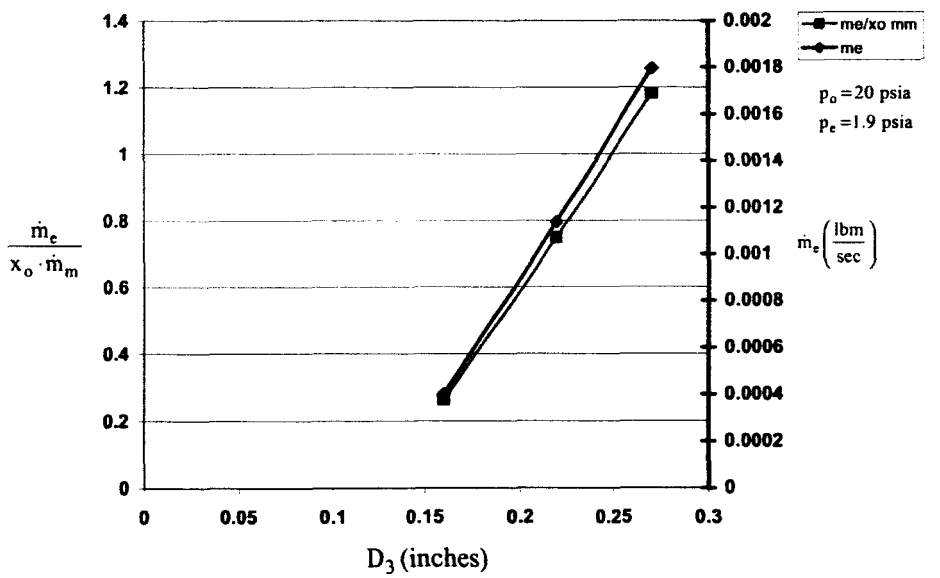

Figure 12. Eductor Evaporator Mass Flow and Entrainment Ratio Sensitivity to Eductor Throat Diameter for Methanol

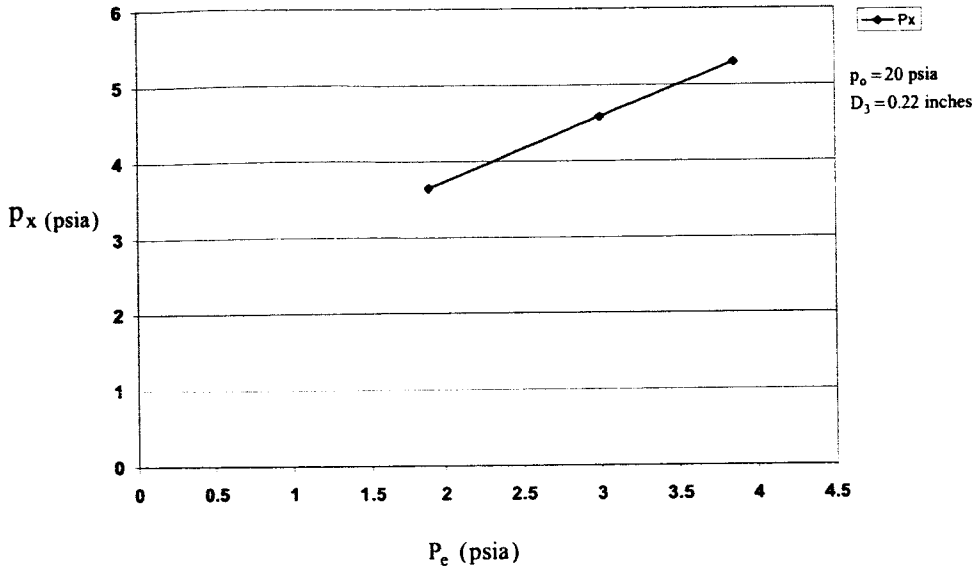

Figure 13. Eductor Exit Pressure Sensitivity to Evaporator Pressure for Methanol

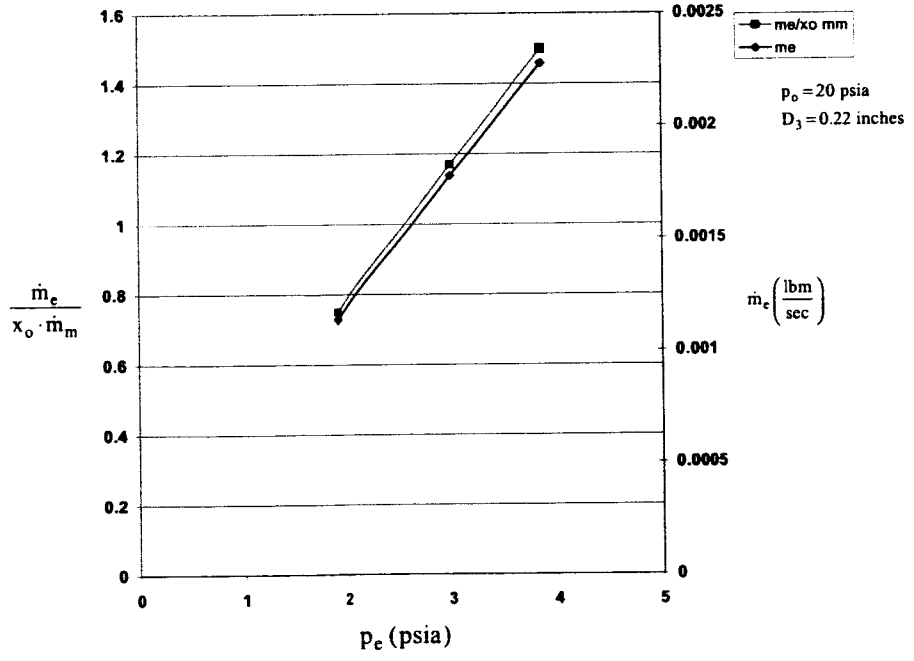

Figure 14. Eductor Evaporator Mass Flow and Entrainment Ratio Sensitivity to Evaporator Pressure for Methanol

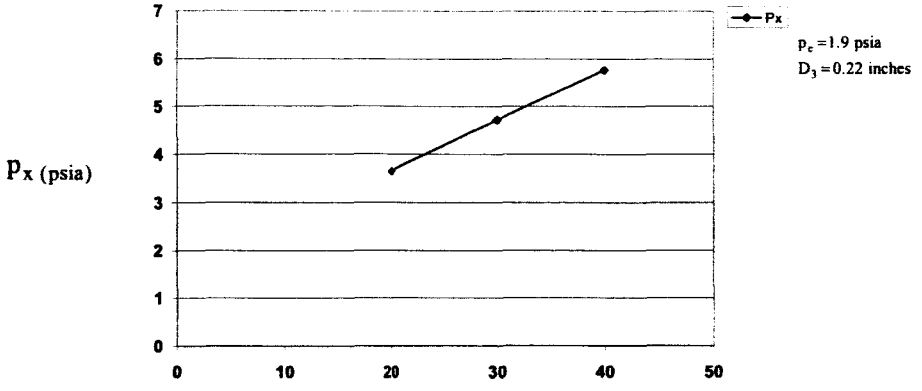

Figure 15. Eductor Exit Pressure Sensitivity to Motive Pressure for Methanol

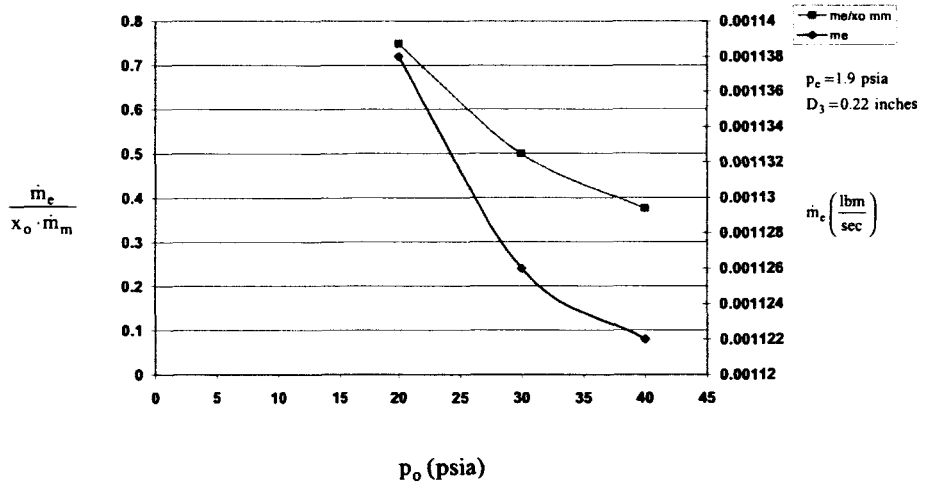

Figure 16. Eductor Evaporator Mass Flow and Entrainment Ratio Sensitivity to Motive Pressure for Methanol

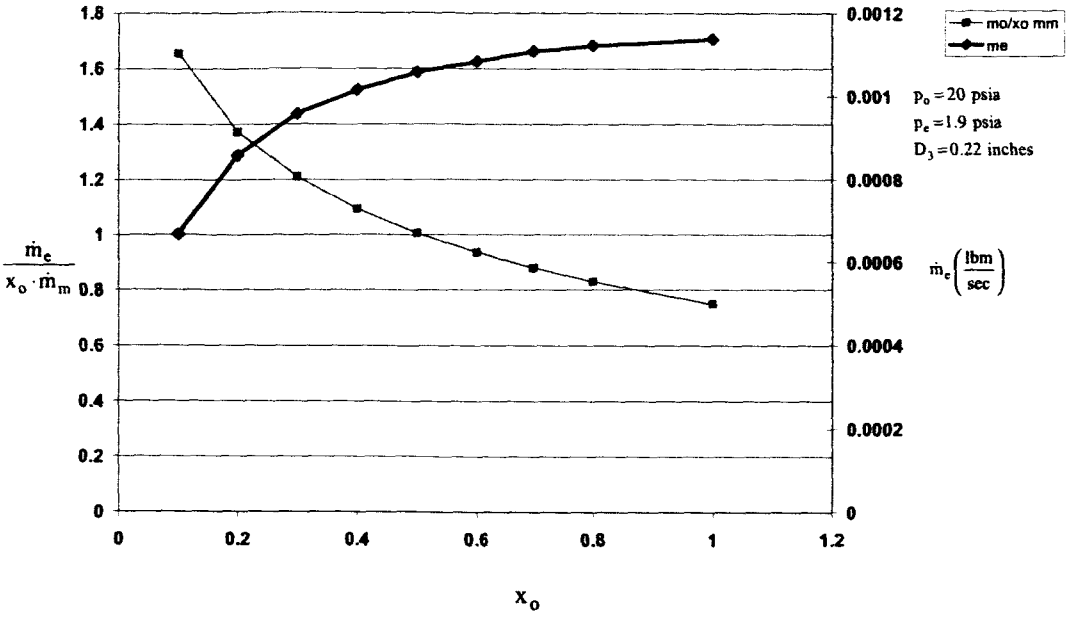

Figure 17. Eductor Evaporator Mass Flow and Entrainment Ratio Sensitivity to Motive Flow Quality for Methanol

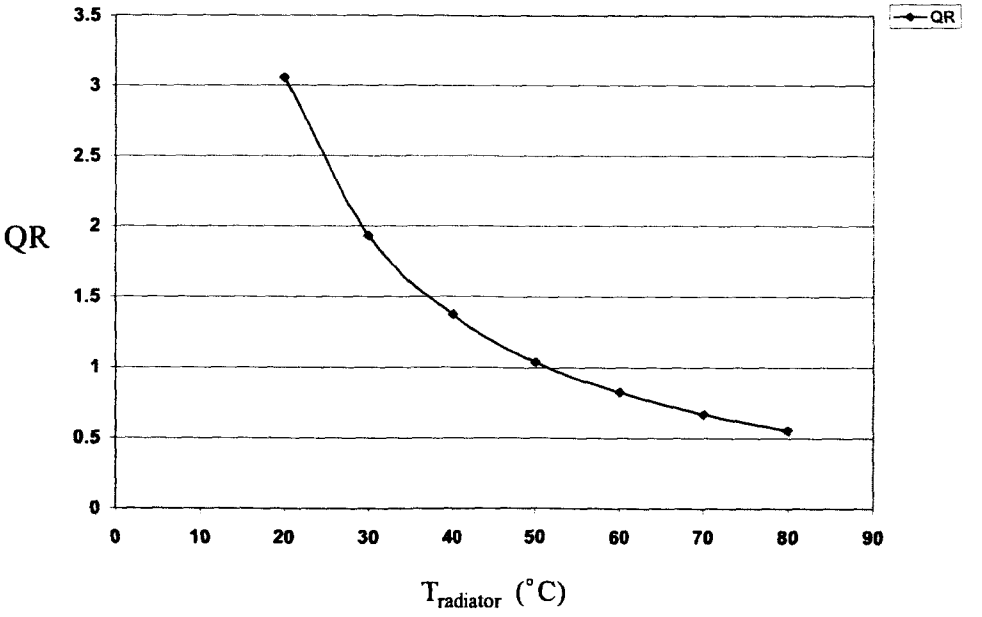

Figure 18. Eductor Efficiency Needed to Offset Supplied LHP Heat Rate

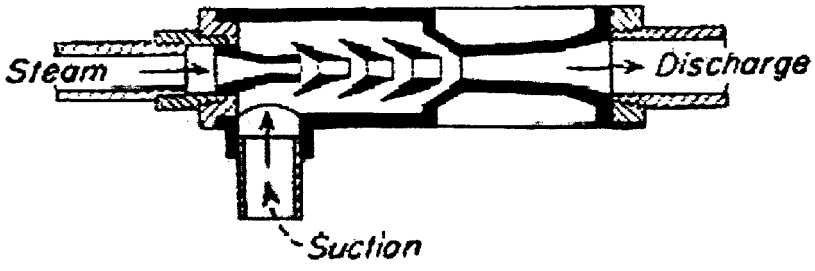

Figure 19. Progressive Suction Eductor

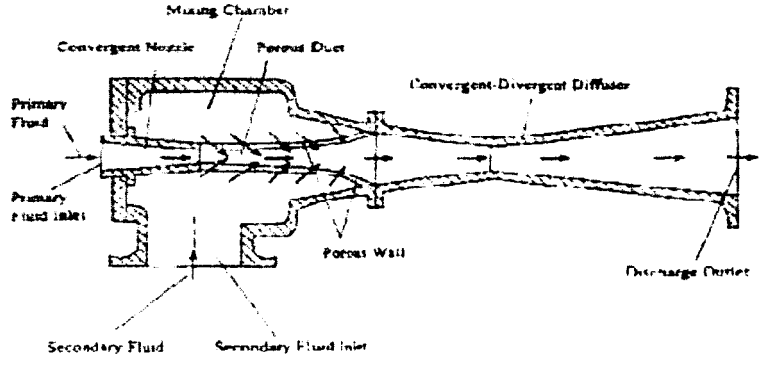

Figure 20. Progressive Suction Eductor using Porous Conical Wall (Cao(17))

Table 1. Analytical Model Results for Water

Flow Quality X0	Motive Pressure P0 psia	Evaporator Pressure Pe psia	Eductor Throat Diameter D3 inches	Eductor Exit Pressure Px psia	Evaporator Mass Flow Rate me lbm/sec	Entrainment Ratio ER
1	50	0.4	0.22	1.829	0.0001842	0.2523
1	50	0.4	0.2	2.132	0.0001499	0.2054
1	50	0.4	0.18	2.536	0.0001206	0.1652
1	50	0.4	0.24	1.595	0.0002264	0.3101
1	50	0.4	0.15	3.492	0.0000762	0.1044
1	50	0.4	0.27	1.337	0.0002945	0.4034
1	50	0.6	0.15	3.671	0.0001193	0.1634
1	50	0.6	0.22	2.011	0.0002832	0.388
1	50	0.6	0.27	1.52	0.0004511	0.6179
1	50	0.8	0.27	1.703	0.0006041	0.8275
1	50	0.8	0.22	2.185	0.0003887	0.5324
1	50	0.8	0.15	3.839	0.0001638	0.2244
1	30	0.4	0.22	1.243	0.0001926	0.4327
1	30	0.4	0.15	2.241	0.0000806	0.1811
1	30	0.4	0.27	0.95	0.0003041	0.6832
1	70	0.4	0.27	1.724	0.0002867	0.2833
1	70	0.4	0.22	2.402	0.0001857	0.1835
1	70	0.4	0.15	4.757	0.0000682	0.0674
0.5	50	0.4	0.22	1.828	0.0001702	0.3377
0.1	50	0.4	0.22		negative	
0.1	50	0.4	0.27	1.337	0.00006219	0.3232
0.3	50	0.4	0.22	1.83	0.000119	0.314
0.7	50	0.4	0.22	1.829	0.0001951	0.3228
0.8	50	0.4	0.22	1.828	0.0002041	0.3144
0.6	50	0.4	0.22	1.83	0.0001853	0.3328

Table 2. Analytical Model Results for Methanol

Flow Quality X0	Motive Pressure P0 psia	Evaporator Pressure Pe psia	Eductor Throat Diameter D3 inches	Eductor Exit Pressure Px psia	Evaporator Mass Flow Rate me lbm/sec	Entrainment Ratio ER
1	20	1.9	0.22	3.647	0.001138	0.7492
1	20	1.9	0.27	3.049	0.001795	1.182
1	20	1.9	0.16	5.231	0.0004	0.2636
1	20	3	0.22	4.579	0.001778	1.17
1	20	3	0.16	6.157	0.0007872	0.5182
1	20	3	0.27	3.99	0.002852	1.877
1	20	3.863	0.27	4.738	0.003654	2.406
1	20	3.863	0.22	5.294	0.00228	1.501
1	20	3.863	0.16	6.771	0.001022	0.6727
1	30	1.9	0.22	4.725	0.001126	0.4992
1	30	1.9	0.27	3.727	0.00183	0.8117
1	30	1.9	0.16	7.345	0.000487	0.216
1	40	1.9	0.16	9.338	0.000469	0.1569
1	40	1.9	0.22	5.767	0.001122	0.3747
1	40	1.9	0.27	4.422	0.001823	0.61
0.8	20	1.9	0.22	3.666	0.001123	0.8309
0.7	20	1.9	0.22	3.664	0.001108	0.8807
0.6	20	1.9	0.22	3.668	0.001085	0.9361
0.5	20	1.9	0.22	3.666	0.001057	1.006
0.4	20	1.9	0.22	3.663	0.001016	1.094
0.3	20	1.9	0.22	3.669	0.000958	1.211
0.2	20	1.9	0.22	3.671	0.000859	1.372
0.1	20	1.9	0.22	3.664	0.000669	1.656

Table 3. Conventional Eductor Performance for Critical Designs

MOTIVE PRESSURE	DISCHARGE PRESSURE	SUCTION PRESSURE	SUCTION CAPACITY
Decrease	Constant	Increase rapidly	Decrease rapidly
Constant	Increase	Increase rapidly	Decrease rapidly
Constant	Constant	Increase	Increase
Constant	Constant	Decrease	Decrease
Increase	Constant	Constant	Decrease gradually
Constant	Decrease	Constant	Unchanged

APPENDIX A-1
Sample EES File for CHP Model

```
FUNCTION sonic(x,p)
"This is Bursik's model of 'metastable sound speed in gas-liquid mixtures' NASA TM 78810"
        if(x<0) then x:=0 else x:=x
        if(x>1) then x:=1 else x:=x
        vL:=volume(steam_NBS,P=P,x=0)
        vG:=volume(steam_NBS,P=P,x=1)
        v:=(1-x)*vL+x*vG
        CpL:=cp(steam_NBS,P=P,x=0)
        Tsat:=temperature(steam_NBS,P=P,x=0)
"CpG=cp(steam_NBS,P=Psat,x=1)"
"EES CP function discontinuous from 11.2 to 11.3 psia"
"Need best EES steam property lookups.  Values are a little off using steam_NBS"
        TH:=Tsat+10
        hG:=enthalpy(steam_NBS,P=P,x=1)
        hH:=enthalpy(steam_NBS,P=P,T=TH)
        cpG:=(hH-hG)/(TH-Tsat)
        Cpbar:=(1-x)*CpL+x*CpG
        T:=Tsat
        TLL:=T-10
        vLL:=volume(steam_NBS,P=P,T=TLL)
        dvdtPL:=(vL-vLL)/(T-TLL)
        TGG:=T+10
        vGG:=volume(steam_NBS,P=P,T=TGG)
        dvdtPG:=(vGG-vG)/(TGG-T)
        dvdtP:=(1-x)*dvdtPL+x*dvdtPG
        PLH:=100*P
        vLH:=volume(steam_NBS,P=PLH,T=Tsat)
        dvdpTL:=(vLH-vL)/(PLH-P)
        PGH:=0.99*P
        vGH:=volume(steam_NBS,P=PGH,T=Tsat)
        dvdpTG:=(vG-vGH)/(P-PGH)
        dvdpT:=(1-x)*dvdpTL+x*dvdpTG
        dpdtV:=-dvdtP/dvdpT
        Cvbar:=Cpbar-T*dvdtP*dpdtV*convert(ft^3-lb_f/lb_m-in^2-F,Btu/lb_m-F)
        gamma:=Cpbar/Cvbar
        sonic:=sqrt(-gamma*v^2/dvdpT*convert(ft^3-lb_f/lb_m-in^2,ft^2/s^2))      "ft/s"
END


"SS Nozzle, Station 0 to t"

"Conservation of Energy"
"h0=ht+Velt^2/2*convert(ft^2/s^2,btu/lb_m)"
"Conservation of Momentum"
"P0*At=mdotm*Velt*convert(ft-lb_m/s^2,lb_f)+Pt*At+tau0*Ax0"
"Conservation of Mass"
"mdotm=At*Velt/vt*convert(in^2,ft^2)"
"State equation"
vt=volume(steam_NBS,P=Pt,h=ht)
h0=enthalpy(steam_NBS,P=P0,x=x0)
Ax0=3.1417*Dt*L0
L0=(D0-Dt)/2/sin(theta0)
Lx0=(D0-Dt)/2/tan(theta0)
v0=volume(steam_NBS,P=P0,x=x0)
betasqrd0=(Dt/D0)^2
```

```
K0=(0.5*sin(theta0)^0.5*(1-betasqrd0)/betasqrd0^2)*(Dt/D0)^4
fnct0=K0*Dt/L0
tau0=fnct0*Vel1^2/8/v1*convert(lb_m/ft-s^2,psia)
x0=quality(steam_NBS,P=P0,h=ht)
s0=entropy(steam_NBS,P=P0,x=x0)
Tt=temperature(steam_NBS,P=Pt,h=ht)
st=entropy(steam_NBS,P=Pt,h=ht)
sonicspeedt=sonic(xt,Pt)
"Input"
x0=1
P0=50
Dt=0.041
At=3.1417*Dt^2/4
D0=0.22
A0=3.1417*D0^2/4
theta0=20
Pt=21.95
mdotm=0.00073
Vel1=1431
st=1.689


"SS Nozzle, Station t to 1"

"Conservation of Energy"
h0=h1+Vel1^2/2*convert(ft^2/s^2,btu/lb_m)
"State equation"
"v1=volume(steam_NBS,P=P1,h=h1)"
"Conservation of Momentum"
mdotm*Vel1*convert(lb-lb_m/s^2,lb_f)+Pt*At=mdotm*Vel1*convert(lb-lb_m/s^2,lb_f)+P1*A1+tau1*Akt
"Conservation of Mass"
mdotm=A1*Vel1/v1*convert(in^2,ft^2)
Akt=3.1417*Dt*Lt
Lt=(D1-Dt)/2/sin(thetat)
Lxt=(D1-Dt)/2/tan(thetat)                    "FlowSystem's info recommends Lxt=7*Dt with thetat=4"
x1=quality(steam_NBS,P=P1,h=h1)
betasqrdt=(Dt/D1)^2
Kt=(2.6*sin(thetat)*(1-betasqrdt)^2/betasqrdt^2)*(Dt/D1)^4
fnct1=Kt*Dt/Lt
tau1=fnct1*Vel1^2/8/v1*convert(lb_m/ft-s^2,psia)
sonicspeed1=sonic(x1,P1)
T1=temperature(steam_NBS,P=P1,h=h1)
s1=entropy(steam_NBS,P=P1,h=h1)
"Input"
D1=0.082
A1=3.1417*D1^2/4
thetat=4


"Vapor flow from evaporator"

"Conservation of Momentum"
Pe*Ae=P2*Ae+mdote*Vele2*convert(ft-lb_m/s^2,lb_f)
"Conservation of Energy"
```

```
he=he2+Vele2^2/2*convert(ft^2/s^2,btu/lb_m)
"Conservation of Mass"
mdote=Ae*Vele2/ve2*convert(in^2,ft^2)
"State equation"
ve2=volume(steam_NBS,P=P2,h=he2)
he=enthalpy(steam_NBS,P=Pe,x=xe)
Te=temperature(steam_NBS,P=Pe,x=xe)
"Input"
Pe=0.4
De=1
Ae=3.1417*De^2/4
xe=1


"Eductor mixing region, stations 1 & 2 to 3"

"Conservation of Momentum"
mdotm*Vel1*convert(ft-lb_m/s^2,lb_f)+mdote*Vele2*convert(ft-lb_m/s^2,lb_f)+P2*A3=mdotc*Vel3*convert(ft-lb_m/s^2,lb_f)+P3
*A3+tau2*Ak2
mdotm*v1+mdote*ve2=mdotc*v12
mdotc=mdotm+mdote
P1=P2
"Conservation of Mass"
mdotc=A3*Vel3/v3*convert(in^2,ft^2)
"State equation"
v3=volume(steam_NBS,P=P3,h=h3)
Ak2=3.1417*D3*L2
L2=(D2-D3)/2/sin(theta2)
betasqrd2=(D3/D2)^2
K2=(0.5*sin(theta2)^0.5*(1-betasqrd2)/betasqrd2^2)*(D3/D2)^4
fnct2=K2*D3/L2
"Using Velbar below cause most of converging flow is evaporator vapor  SS nozzle exit flow not in contact with walls"
tau2=fnct2*Velbar2^2/8/v3*convert(lb_m/ft-s^2,psia)
Velbar2=(Vele2+Vel3)/2
sonicspeed3=sonic(x3,P3)
s3=entropy(steam_NBS,P=P3,h=h3)
"Input"
D3=0.22
A3=3.1417*D3^2/4
theta2=20
D2=0.43


"From stations 0 & E to 3"

"Conservation of Energy"
mdotm*h0+mdote*he=mdotc*h3+mdotc*Vel3^2/2*convert(ft^2/s^2,btu/lb_m)
T3=temperature(steam_NBS,P=P3,h=h3)
x3=quality(steam_NBS,P=P3,h=h3)


"From station 3 to x"

"Conservation of Energy"
```

```
h3+Vel3^2/2*convert(ft^2/s^2,btu/lb_m)=hx+Velx^2/2*convert(ft^2/s^2,btu/lb_m)
"Conservation of Momentum"
mdotc*Vel3*convert(ft-lb_m/s^2,lb_f)+P3*A3=mdotc*Velx*convert(ft-lb_m/s^2,lb_f)+Px*A3+tau3*Ak3
"Conservation of Mass"
mdotc=Ax*Velx/vx*convert(in^2,ft^2)
"State equation"
vx=volume(steam_NBS,P=Px,h=hx)
Ak3=3.1417*D3*L3
L3=(Dx-D3)/2/sin(theta3)
betasqrd3=(D3/Dx)^2
K3=2.6*sin(theta3)*(1-betasqrd3)^2/(betasqrd3^2)*(D3/Dx)^4
fnct3=K3*D3/L3
tau3=fnct3*Vel3^2/8/v3*convert(lb_m/ft-s^2,psia)
xx=quality(steam_NBS,P=Px,h=hx)
Tx=temperature(steam_NBS,P=Px,h=hx)
Txsatv=temperature(steam_NBS,P=Px,x=1)
sx=entropy(steam_NBS,P=Px,h=hx)
"Input"
P3=1
Dx=0.93
Ax=3.1417*Dx^2/4
theta3=4

ER=mdote/(x0*mdotm)
```

Unit Settings: [F]/[psia]/[lbm]/[degrees]

A0 = 0.03801 [in^2]	A1 = 0.005281 [in^2]	A3 = 0.03801 [in^2]
Ae = 0.7854 [in^2]	Ak0 = 0.03371 [in^2]	Ak2 = 0.2122 [in^2]
Ak3 = 3.517 [in^2]	Akt = 0.03785 [in^2]	At = 0.00132 [in^2]
Ax = 0.6793 [in^2]	betasqrd0 = 0.03473	betasqrd2 = 0.2618
betasqrd3 = 0.05596	betasqrdt = 0.25	D0 = 0.22 [in]
D1 = 0.082 [in]	D2 = 0.43 [in]	D3 = 0.22 [in]
De = 1 [in]	Dt = 0.041 [in]	Dx = 0.93 [in]
ER = 0.2523	fnct0 = 0.04422	fnct2 = 0.1547
fnct3 = 0.006987	fnctt = 0.01423	h0 = 1174 [Btu/lb$_m$]
h1 = 1038 [Btu/lb$_m$]	h3 = 1127 [Btu/lb$_m$]	he = 1093 [Btu/lb$_m$]
he2 = 1093 [Btu/lb$_m$]	ht = 1133 [Btu/lb$_m$]	hx = 1158 [Btu/lb$_m$]
K0 = 0.2823	K2 = 0.2159	K3 = 0.1816
Kt = 0.102	L0 = 0.2617 [in]	L2 = 0.307 [in]
L3 = 5.089 [in]	Lt = 0.2939 [in]	Lx0 = 0.2459 [in]
Lxt = 0.2932 [in]	mdotc = 0.0009142 [lb$_m$/s]	mdote = 0.0001842 [lb$_m$/s]
mdotm = 0.00073 [lb$_m$/s]	P0 = 50 [psia]	P1 = 0.3998 [psia]
P2 = 0.3998 [psia]	P3 = 1 [psia]	Pe = 0.4 [psia]
Pt = 21.95 [psia]	Px = 1.829 [psia]	s0 = 1.659 [Btu/lb$_m$-R]
s1 = 1.953 [Btu/lb$_m$-R]	s3 = 2.014 [Btu/lb$_m$-R]	sonicspeed1 = 1186 [ft/s]
sonicspeed3 = 1262 [ft/s]	sonicspeedt = 1448 [ft/s]	st = 1.689 [Btu/lb$_m$-R]
sx = 1.996 [Btu/lb$_m$-R]	T1 = 72.83 [F]	T3 = 148.6 [F]
tau0 = 0.136 [psia]	tau2 = 0.004723 [psia]	tau3 = 0.000818 [psia]
taut = 0.04378 [psia]	Te = 72.84 [F]	theta0 = 20 [degrees]
theta2 = 20 [degrees]	theta3 = 4 [degrees]	thetat = 4 [degrees]
Tt = 232.9 [F]	Tx = 218.4 [F]	Txsatv = 122.7 [F]
v0 = 8.523 [ft^3/lb$_m$]	v1 = 131.2 [ft^3/lb$_m$]	v12 = 264.4
v3 = 361.8 [ft^3/lb$_m$]	ve2 = 792.2 [ft^3/lb$_m$]	Vel1 = 2612 [ft/s]
Vel3 = 1253 [ft/s]	Velbar2 = 639.8 [ft/s]	Vele2 = 26.75 [ft/s]

V_{eff} = 1431 [ft/s]	V_{ebx} = 42.72 [ft/s]	v_t = 17.96 [ft^3/lb_m]
v_x = 220.5 [ft^3/lb_m]	x_0 = 1	x_1 = 0.948
x_3 = 100	x_e = 1	x_t = 0.9743
x_x = 100		

APPENDIX B

Shearography for Nondestructive Inspection

with applications to

BAT Mask Tile Adhesive Bonding and Specular Surface Honeycomb Panels

Final Report

To: NASA Goddard Space Flight Center
(Grant number NCC5-508)

Submitted by:
Daniel B. Lysak
The Applied Research Laboratory
The Pennsylvania State University
10 February 2003

Shearography
for
Nondestructive Inspection

Abstract
In this report we examine the applicability of shearography techniques for nondestructive inspection and evaluation in two unique application areas. Shearography is shown to give good results in evaluating the quality of adhesive bonds holding lead tiles to the Swift BAT gamma ray mask. Using a vibration excitation, poorly bonded tiles can be readily distinguished from those that are well bonded. The shearography results are compared with pull tests performed on a set of tile samples. The second application is to evaluate the bonding between the skin and core of a specular surface honeycomb structure. A novel technique is presented that allows specular objects to be evaluated using shearography. The technique readily identifies large scale bond failures in the panel, although some scaling issues regarding the particulars of the panel need further examination.

1. Introduction

The goal of this project is to evaluate the applicability of shearography for nondestructive inspection and evaluation (NDI / NDE) of certain mission critical components. This work was performed as part of a Cooperative Agreement with the NASA Goddard Space Flight Center (GSFC), grant number NCC5-508. Two potential application areas were identified:

1. For tiles on the Swift BAT gamma ray mask, to determine whether poorly-bonded tiles could be distinguished from well-bonded tiles.
2. To determine whether shearography could identify any bonding failure between the skin and the core of specular-surface honeycomb structures.

The Penn State University Applied Research Lab (PSU/ARL) provided the shearography system and labor while the GSFC provided the test samples and consultation regarding sample construction and appropriate test environments.

Shearography, a form of speckle shear interferometry, is a robust yet sensitive technique for NDI / NDE that has been demonstrated to be effective in the field environment out of the laboratory. [1] Unlike holographic methods, which measure absolute surface displacements and are very sensitive to environmental disturbances, shearography is a differential technique that measures changes in surface gradient due to applied excitation stress. As such, it provides a common mode rejection that makes it relatively insensitive to environmental conditions. While shearography has been around for some time, the phase shifting technique used in the PSU/ARL system provides greatly improved visualization of results by computing the speckle phase instead of merely using the speckle image, as in earlier methods. [2]

The two application areas require different methods of generating the excitation stress. In the case of the BAT mask tiles, the adhesive holding the tile is somewhat flexible, and if we apply a low amplitude vibration in the plane of the mask, the tile tends to tilt back and

forth slightly. The amplitude of this motion depends inversely on how well the tile is bonded to the surface of the mask. By taking two snapshots, 180° apart at the extremes of the tile vibration cycle, the shearography system measures the amplitude of motion as the change in slope of the tile surface.

For honeycomb panels shearography has been demonstrated to give good results in identifying bonding failures between the core and skin under vacuum, pressure, and even thermal excitation. At the cell walls of the honeycomb core, where the skin is attached, the surface is constrained, and there is no change in the surface slope when the excitation is applied. However, at the interior of the cells there is nothing holding the skin, so the surface slope is free to change under the excitation, and, when the differential surface gradient is displayed, it will appear different from the constrained areas. If the structure is sound, the distinct honeycomb pattern of the core will appear in the display, and any bonding failure will be readily apparent as an interruption of that pattern. In the present application, however, the challenge is that the panels have a specular (mirror-like) finish and do not produce the speckle patterns needed for shearography. (Note that the terms "specular" and "speckle" have an unfortunate phonetic similarity which can often be the source of some confusion.) In this case the speckles can be generated by illuminating some other diffuse surface with laser light and then use the specular surface as a mirror to view them. In principle, this configuration should produce a display very similar to that obtained from a diffuse surface honeycomb panel.

In Section 2 below, we review the principles of shearography and describe the basic PSU/ARL system configuration and operation. In Sections 3 and 4 we discuss in detail the two application areas, the BAT mask tiles and the specular honeycomb panel, respectively. These sections include the experimental set up for each case and results obtained. Finally in Section 5 we present our conclusions and recommendations.

2. Technical Background

Shearography makes use of the "subjective" speckle pattern [3] that is produced through random interference when the rough surface of an object is illuminated by coherent laser light and imaged through a lens. The speckle image is "sheared" by splitting the wave front into two parts which are then recombined at the image plane with a small transverse shift between them. The effect is that each point in the image plane is the image of two different scattering points on the rough surface separated by the shear vector (dx, dy). The speckle intensity at the image point depends on the interference between these two scattering points. The speckle pattern produced is highly sensitive to differential out-of-plane displacements over the shear distance but relatively insensitive to common mode displacements. As a result, shearography provides a technique for measuring small changes in surface slope that is robust enough to operate outside the laboratory environment.

The PSU/ARL shearography system is illustrated in Figure 1 below. It uses a Coherent DPSS-532 diode-pumped Nd:YAG continuous wave (CW) laser producing 500 mW output at 532 nm as the illumination source with a Pulnix TM-1040 Progressive Scanning High Resolution camera (960 x 640 pixels) interfaced through a Bitflow RoadRunner

frame grabber to record the speckle images. Speckle shearing is produced using a Michelson interferometer arrangement with one of the mirrors tilted, and the shear distance is set by adjusting the degree of tilt. A 486-based lunchbox computer is used to acquire the camera images, process the data, and display the results as well as for overall control and synchronization of the various subsystems.

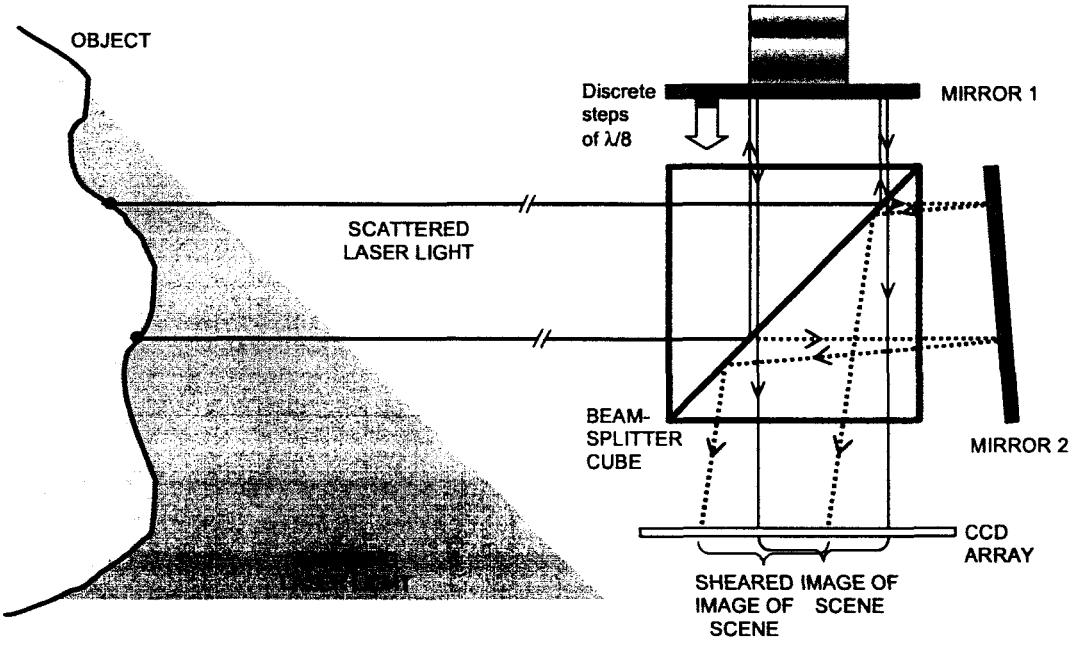

Figure 1. Basic PSU/ARL shearography system, based on a Michelson interferometer with phase stepping. The piezo-electric actuator (PZT) controls the stepping of mirror 1, while the shear distance is determined by the tilt in mirror 2. The imaging lens, located between the beam splitter cube and the CCD array, is not shown.

Generally speaking, nondestructive evaluation is done by observing the changes when some small excitation is applied to the object under test. Various types of excitation, such as pressure, heat, force, vibration, and others, may be used depending on the particular application. With shearography, the changes in the observed speckle pattern infer changes in the surface gradient component in the direction of the shear displacement. Two speckle images, representing the reference and excited states, can be subtracted to produce a visualization of the gradient changes. However, better immunity to variations in surface reflectivity and other noise effects can be obtained by first obtaining the speckle phase at each pixel for both the reference and the excitation conditions, and then computing the phase difference pixel by pixel. This produces a much clearer visualization image, and the result is a more quantitative representation of the change in gradient.

In the PSU/ARL shearography system, speckle phase is computed using a highly accurate, four-step, phase-stepping approach in which four separate images are taken at

different interferometric path differences, in quarter wavelength increments. Phase stepping is performed by moving one of the interferometer mirrors (mirror 1 in Figure 1) using a piezo-electric actuator controlled by a waveform generator board in the computer. The intensity at pixel (x,y) in each of the four images can be represented by

$$I_1(x,y) = a(x,y) + b(x,y)\cos[\phi(x,y)]$$
$$I_2(x,y) = a(x,y) + b(x,y)\cos[\phi(x,y) + \pi/2]$$
$$I_3(x,y) = a(x,y) + b(x,y)\cos[\phi(x,y) + \pi]$$
$$I_4(x,y) = a(x,y) + b(x,y)\cos[\phi(x,y) + 3\pi/2], \quad (1)$$

where $f(x,y)$ is the speckle phase, which is directly related to differential optical path length through the two scattering points. The bias intensity, $a(x,y)$, and fringe modulation intensity, $b(x,y)$, account for variations in illumination, surface reflectivity, and other effects. Solving for the speckle phase, the $a(x,y)$ and $b(x,y)$ terms drop out of the solution, and we get

$$\varphi(x,y) = \tan^{-1}\left[\frac{I_2(x,y) - I_4(x,y)}{I_1(x,y) - I_3(x,y)}\right]. \quad (2)$$

If the shearing distance is small and the illumination and viewing directions are nearly normal to the object surface, the change in speckle phase can be approximately related to the differential displacement by

$$\Delta\phi(x,y) = \phi_e(x,y) - \phi_r(x,y)$$
$$= \frac{4\pi}{\lambda}(\delta z_e - \delta z_r) \quad (3)$$

where $f_e(x,y)$ and $f_r(x,y)$ are the speckle phase for the excitation and reference conditions, respectively, computed using Equation 1. The dz_e and dz_r terms represent the out-of-plane differences between the two points on the object surface that image to pixel (x,y), for the excitation and reference conditions, respectively. It should be noted that the speckle phase as computed by Equation 1 ranges from 0 to 2p and may have 2p jumps, giving the resulting difference image a fringe-like appearance. If a true quantitative measurement is desired, it may be necessary to do some post-processing with a phase unwrap algorithm.

3. BAT Mask Tile Adhesive Bonding

The first application area to be evaluated involves the quality of the adhesive bonds that attach the tiles to the Swift BAT mask. The goal is to determine whether shearography methods can distinguish the poorly bonded tiles from those that are well bonded. The mask contains about 52,000 lead tiles arranged in a pseudo-random pattern, and each tile is approximately 5 mm square, 1 mm thick, and weighs about 0.25 grams. The excitation stress is a low amplitude vibration in the plane of the mask surface. The adhesive used to bond the tiles to the mask surface is somewhat flexible, and the combination of tile and adhesive can be roughly modeled as a mass on a spring that would respond to the vibration by swaying back and forth, as illustrated in Figure 2 below. The quality of the bond relates to the stiffness of the spring, which in turn determines the amplitude of motion. Based on the tile mass and a very rough estimate of the adhesive spring constant,

the optimal excitation frequency was expected to be in the range of a few tens to a few hundreds of Hertz.

Good results were obtained with an excitation frequency of 180 Hz, although the exact value did not appear to be critical. The "reference" and "excitation" conditions were taken to be at 120° and -60° in the vibration cycle, representing the points where the tiles had the greatest tilt. These phase angles are with respect to the output signal of the waveform generator and compensate for any phase shift due to the shaker and the tile-"spring" combination. (Note that there are two unrelated meanings of the word phase that we are using: the speckle phase and the phase of the vibration cycle.) A set of four phase-stepped speckle images is captured both at the "reference" and at the "excitation" by strobing the laser illumination at these points in the vibration cycle. A strobe duty cycle of 25% is a good compromise between maximizing light energy to the camera and not blurring the speckle images. The speckle phase maps for each condition are then computed, and the absolute difference between the two shows the amplitude of motion at each tile.

Figure 2. BAT mask tiles under vibration excitation. The "reference" and "excitation" conditions are taken to be two points in the vibration cycle, 180° apart, which give the extremes of tile tilt.

The test configuration is illustrated in Figure 3. Each image is captured with the camera operating in time-integration mode over a number of laser strobe pulses, which are synchronized with the desired vibration phase angle, reference or excitation. An integration time of 160 msec with a vibration excitation of 180 Hz provides for integration over 28 to 29 strobe pulses. Since the aperture of the camera lens must be stopped down to f/16 to get a large enough speckle size, this allows sufficient light to be accumulated for good speckle images. The strobe is generated by gating the CW laser using an acoustic-optic modulator (AOM) to direct the beam through a pin hole and onto the BAT mask. The AOM is controlled through a PC Instruments PCI-312 dual channel waveform generator board in the computer, which is also used to produce the vibration signal.

It has been assumed here that the motion of a tile under vibration is regular in the steady state so that its displacement is always the same at any particular phase angle of the vibration cycle. If this were not the case the speckles would be decorrelated over the set of strobe pulses and would tend to be smeared out. This assumption has been confirmed.

(It should be noted that in cases where this assumption does not hold, the smeared speckles might provide an alternate method for identification of poorly bonded tiles.)

The vibration signal is a cosine function produced by the waveform generator board and coupled through an external power amplifier to a mechanical shaker, which drives the vibration of the BAT mask. This arrangement provides for synchronization with the acousto-optic modulator and the camera as well as allowing for the selection of all the critical parameters through the computer interface, including the frequency and amplitude of vibration and the strobe phase and dwell time.

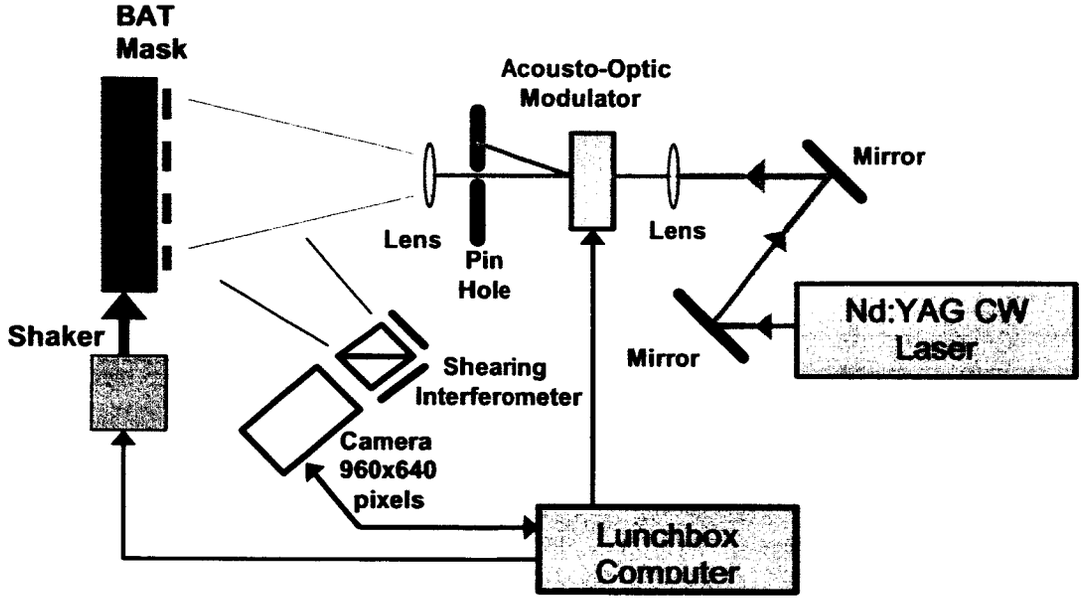

Figure 3. BAT mask test configuration. The shaker vibrates the BAT mask assembly while the acoustic-optic modulator is used to create a strobe effect with the laser beam by directing it through the pinhole and onto the mask at the appropriate point in the vibration cycle.

The experimental set up is shown in Figure 4. The BAT mask and shaker (the red and white object) are at the back toward the right side. The camera and interferometer are at the back on the left side. The acousto-optic modulator is at the right front, and the pinhole and lens are between the acousto-optic modulator and the BAT mask. The laser is not shown. A close up of the BAT mask, illuminated by the laser, with the shaker to its right is shown in Figure 5. To provide a reasonable light level for the camera the laser illumination area was chosen to be about 15 cm in diameter. It should be noted that gating with a CW laser is a rather inefficient since the duty cycle only 25%. The acoustic-optic modulator also introduces inefficiencies in that only one of the diffraction lobes can be utilized. A possible alternative would be to use a pulsed laser whose pulse could be externally controlled by the computer.

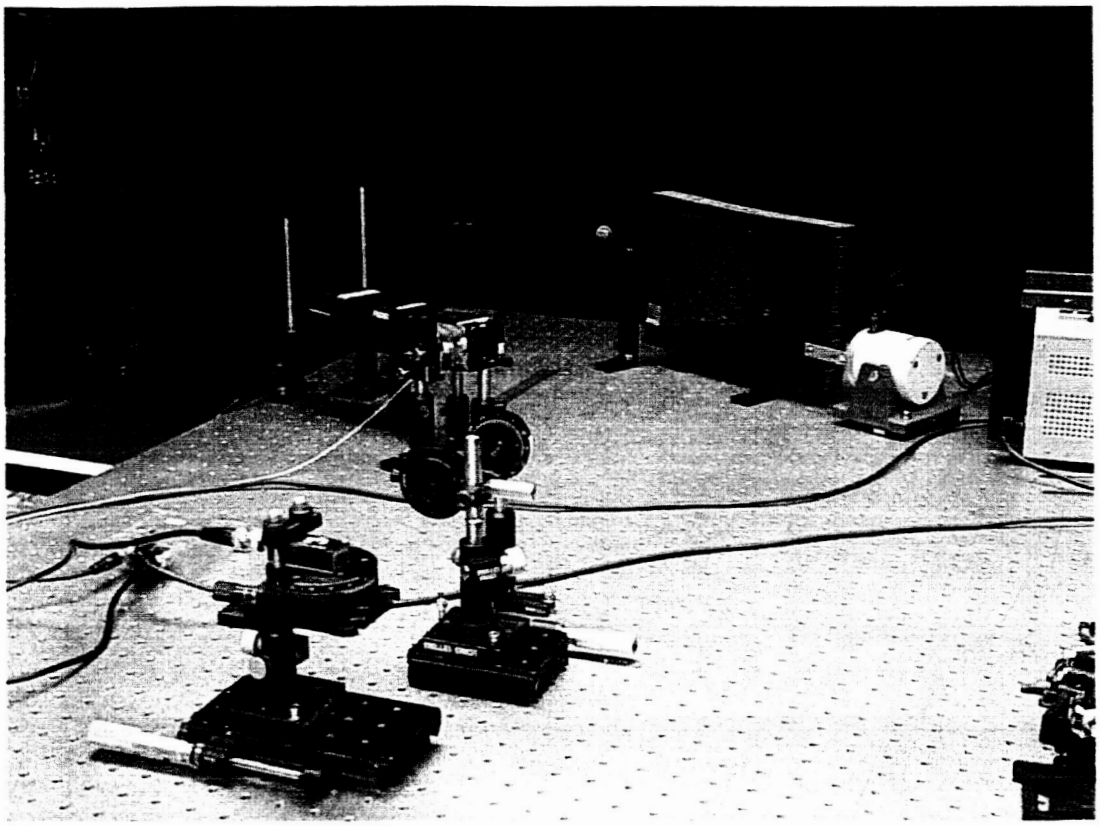

Figure 4. Experimental set up. The BAT mask is in the back with the shaker (the red and white object) to the right of it. The camera and interferometer are in the back at the left, and the acousto-optic modulator is at the left front. The pinhole and lens are between the acousto-optic modulator and the BAT mask. The laser is not shown here.

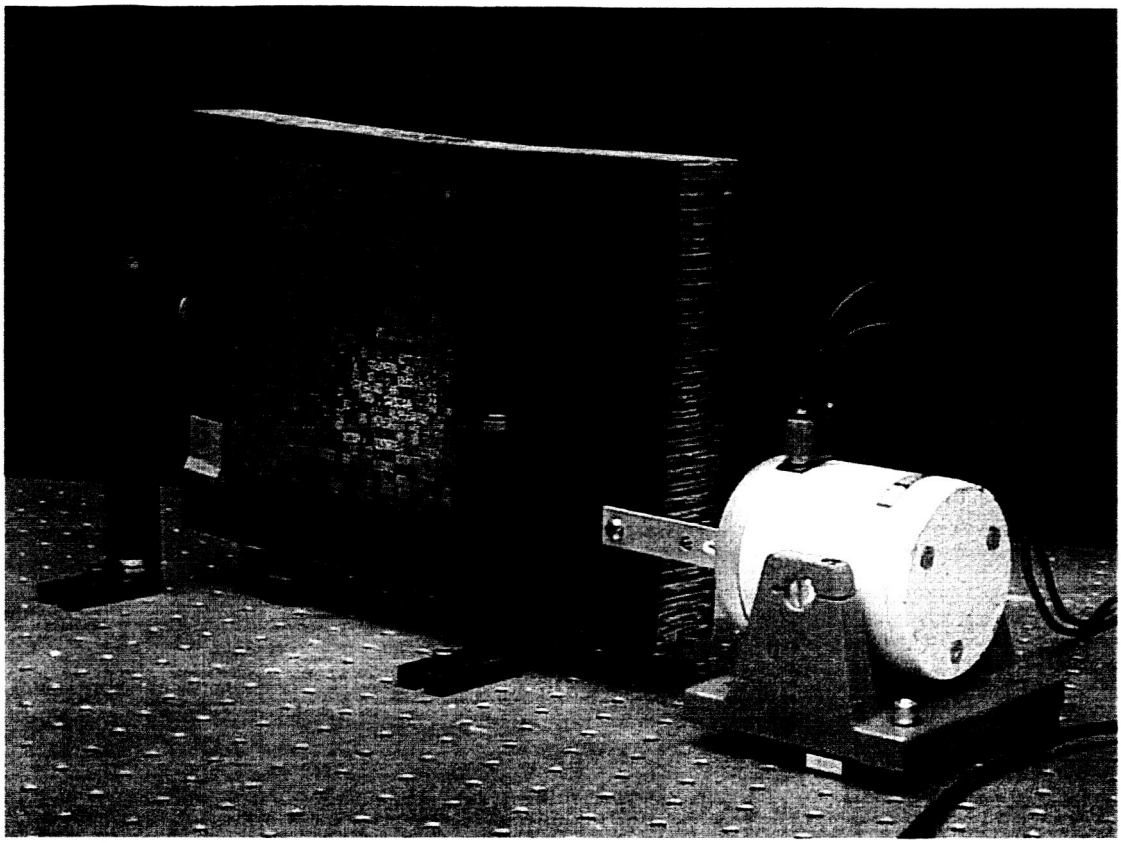

Figure 5. A test portion of the BAT mask, illuminated by laser light, attached to a mechanical shaker. The tiles appear as a pseudo-random pattern of small gray squares. The orange spots are patches of adhesive where the tiles have fallen off.

Figure 6 shows a sheared white light image of the BAT mask as seen through the interferometer by the camera. The horizontal shear displacement, which is about 1 mm (20% of the tile size), makes the image looks blurred. Figure 7 is a sheared image captured in laser light, illustrating the speckle inherent in such an image. Also apparent in this image is the limit of laser illumination, the roughly circular area in the right two-thirds of the picture, where good results can be obtained. This particular image corresponds to the first phase step for the reference condition (at 120° in the vibration cycle). Three other speckle phase step images, which are not shown, are also taken for the reference condition. These would look the same as the first image but are actually quite different in the speckle pattern detail. These four images are then used to compute a speckle phase map for the reference condition, which is shown in Figure 8. Notice that in the phase map, individual tiles are not seen, indicating that effects due to variations in illumination and reflectivity across the surface are removed when the speckle phase is computed.

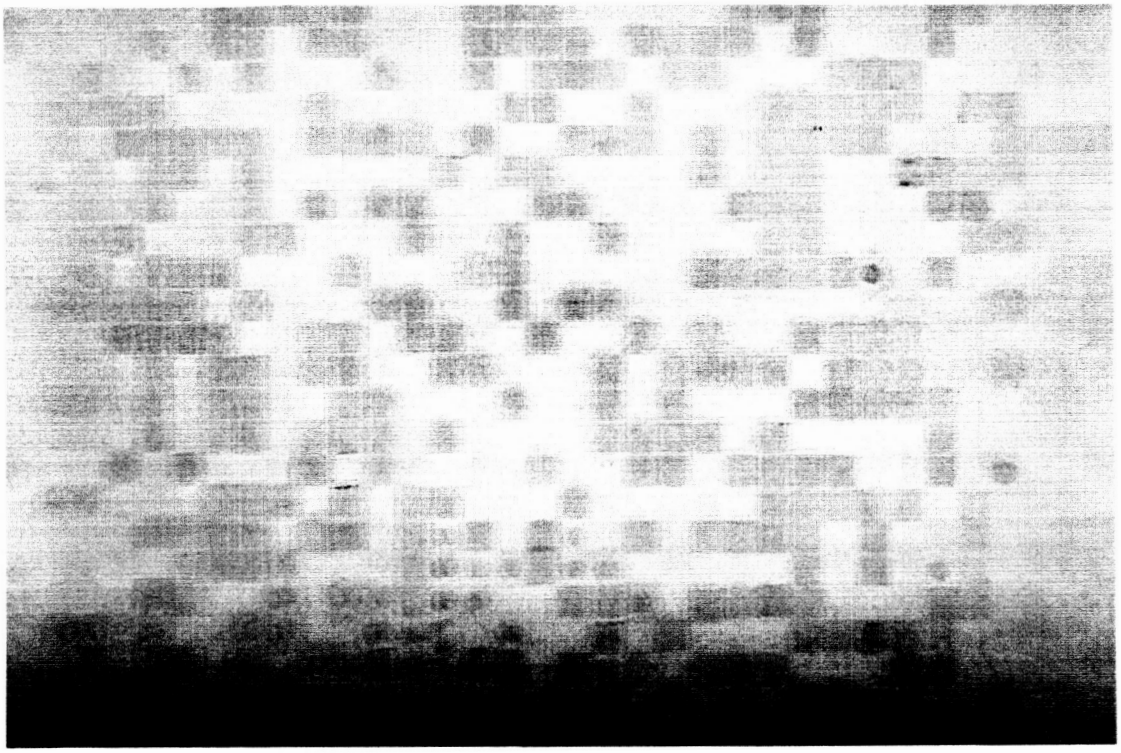

Figure 6. Image of the BAT mask taken in white light as seen through the interferometer by the camera. The image is sheared horizontally by about 1 mm making it appear blurred.

The phase map for the excitation condition (at -60 degrees in the vibration cycle) would appear very similar to the one in Figure 8 for the reference; however, they are again quite different in the speckle details. The differential displacement, which is shown in Figure 9, is obtained by taking the absolute difference, pixel by pixel, of the reference and excitation speckle maps. The tiles with the greatest range of motion are readily apparent against the almost uniform dark background in this figure. Note that the region with the dark background is the area where there is sufficient illumination. Dark areas, with differential displacement close to zero, represent those parts of the mask where there is no change in the phase map, which implies no (or very little) change in the surface slope. These may be areas with no tiles or with tiles that are very well bonded. In the outer portion of the figure (the area with the speckle background), the illumination is not strong enough to produce a good phase map, and the speckle there is useless noise.

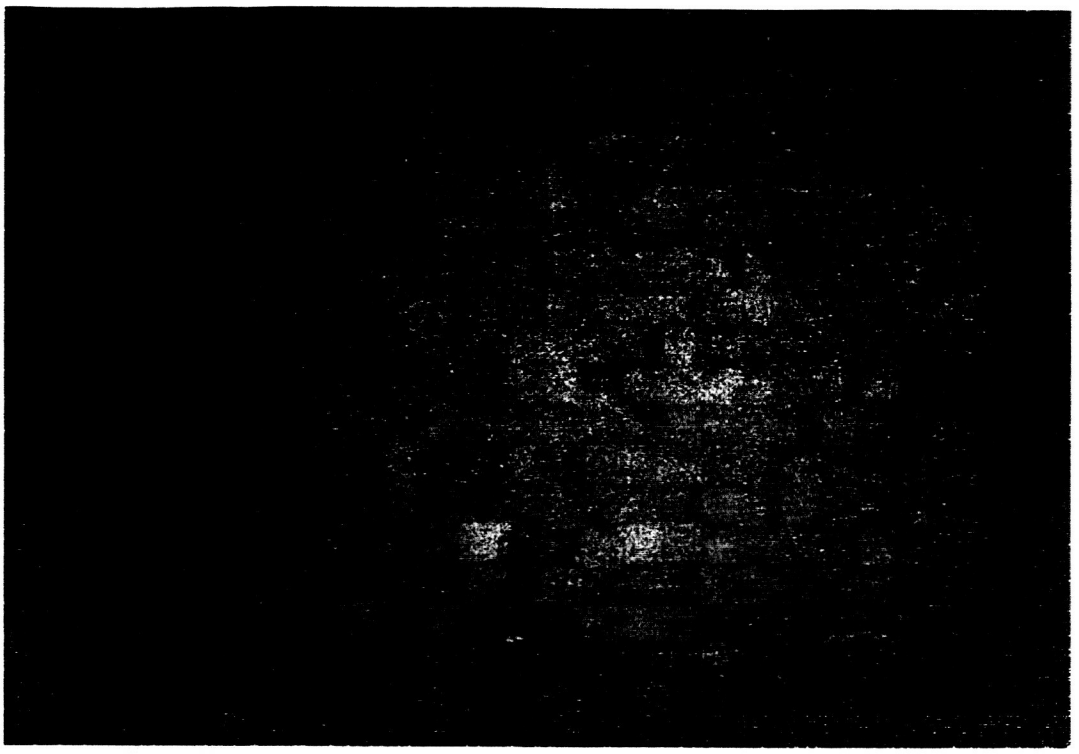

Figure 7. Typical sheared image of the mask acquired under laser light. This particular image is for the reference condition (at 120 degrees in the vibration cycle) and is the first in the series of four phase-stepped images for that condition. All the images of this type appear to be identical but are actually quite different in the speckle pattern details.

The figures described here were obtained at a vibration frequency of 180 Hz. It was anticipated that tiles with different quality bonding might respond differently to different excitation frequencies. We note, however, that results appeared fairly uniform over a range of frequencies, and no strongly resonant features were apparent. This might be because the emphasis during testing was on visual identification of loose tiles (see the discussion below on the pull test) or because the test did not cover a broad enough range of frequencies.

Generally speaking, the vibration amplitude seemed to be more critical than the frequency. For good identification the amplitude must be set low enough that no motion appears in either the well bonded tiles or the background structure to which the tiles are attached. This allows the poorly bonded tiles to clearly stand out in the differential displacement image. As a practical matter the amplitude is not well regulated by the voltage output from the waveform generator because of variation in the frequency response of the shaker. However, a reasonable adjustment can be obtained by turning up the amplitude until motion is seen throughout the whole imaged area, including the background structure, and then backing off.

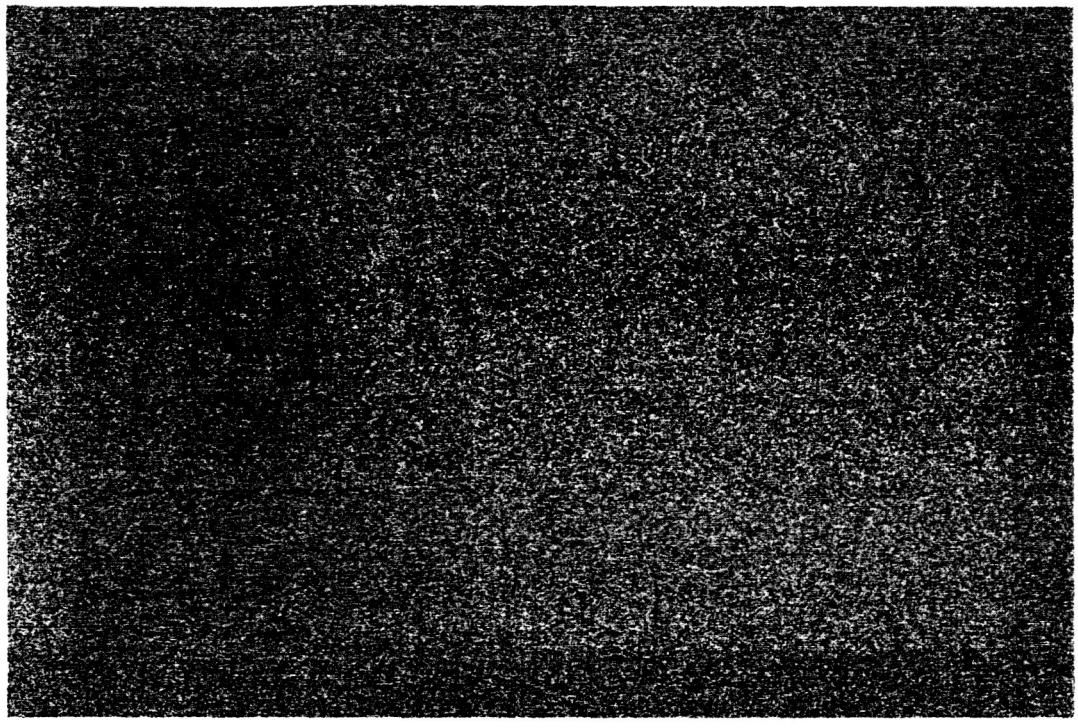

Figure 8. Speckle phase map computed from the four phase-stepped images for the reference condition (120 degrees in the vibration cycle). The phase map for the excitation condition has the same general appearance, but again the details are quite different. The vibration frequency is 180 Hz.

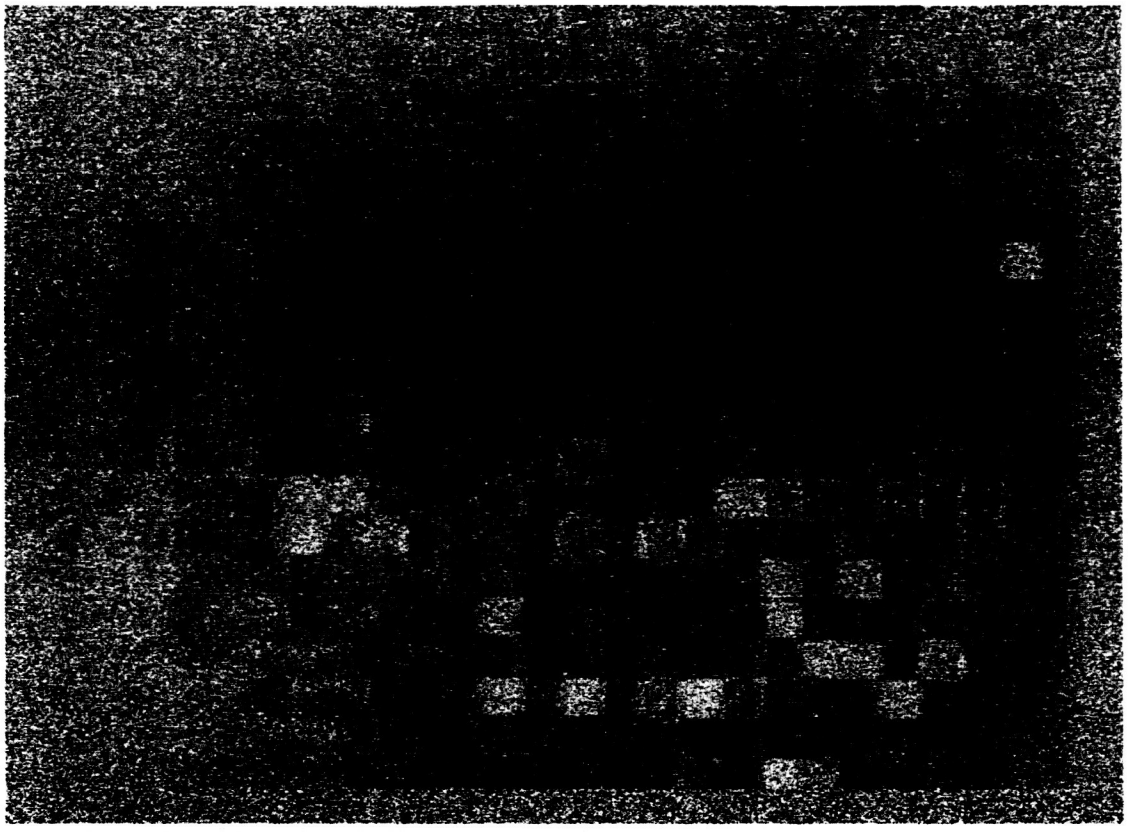

Figure 9. Differential displacement, computed by taking the difference between the reference and excitation speckle phase maps (120 and -60 degrees in the vibration cycle, respectively). The area with the dark background is the region with sufficient illumination. Those tiles that have the greatest range of motion stand out against the relatively uniform dark background in that region. The vibration frequency is 180 Hz.

In many inspection applications, shearography is used to visually identify whether or not the object has failed, and all of the poorly bonded tiles stand out pretty clearly in Figure 9. In order to put the results on a more quantitative basis, a pull test was performed on a number of tiles for comparison with the shearography results. To assure a straight pull, a flat head nail was attached to the tiles with super glue as a pull mechanism. As each tile was pulled to failure, the force was measured with a load cell and automatically stored on computer for analysis. A scatter graph of pull force versus the shearography differential displacement, where each point represents a tile, is shown in Figure 10. The differential displacement was computed from the gray scale image of Figure 9 by averaging over an 11 x 11 block of pixels at the center of each tile. A nearly inverse relationship is apparent in the graph. The graph of inverse differential displacement (bottom of Figure 10) then becomes roughly linear, although the points spread out at the upper end because the displacement becomes small there and random error is accentuated in the inverse. It is anticipated that increasing the vibration amplitude would generally increase the differential displacement of all the tiles, resulting in a tighter linear fit.

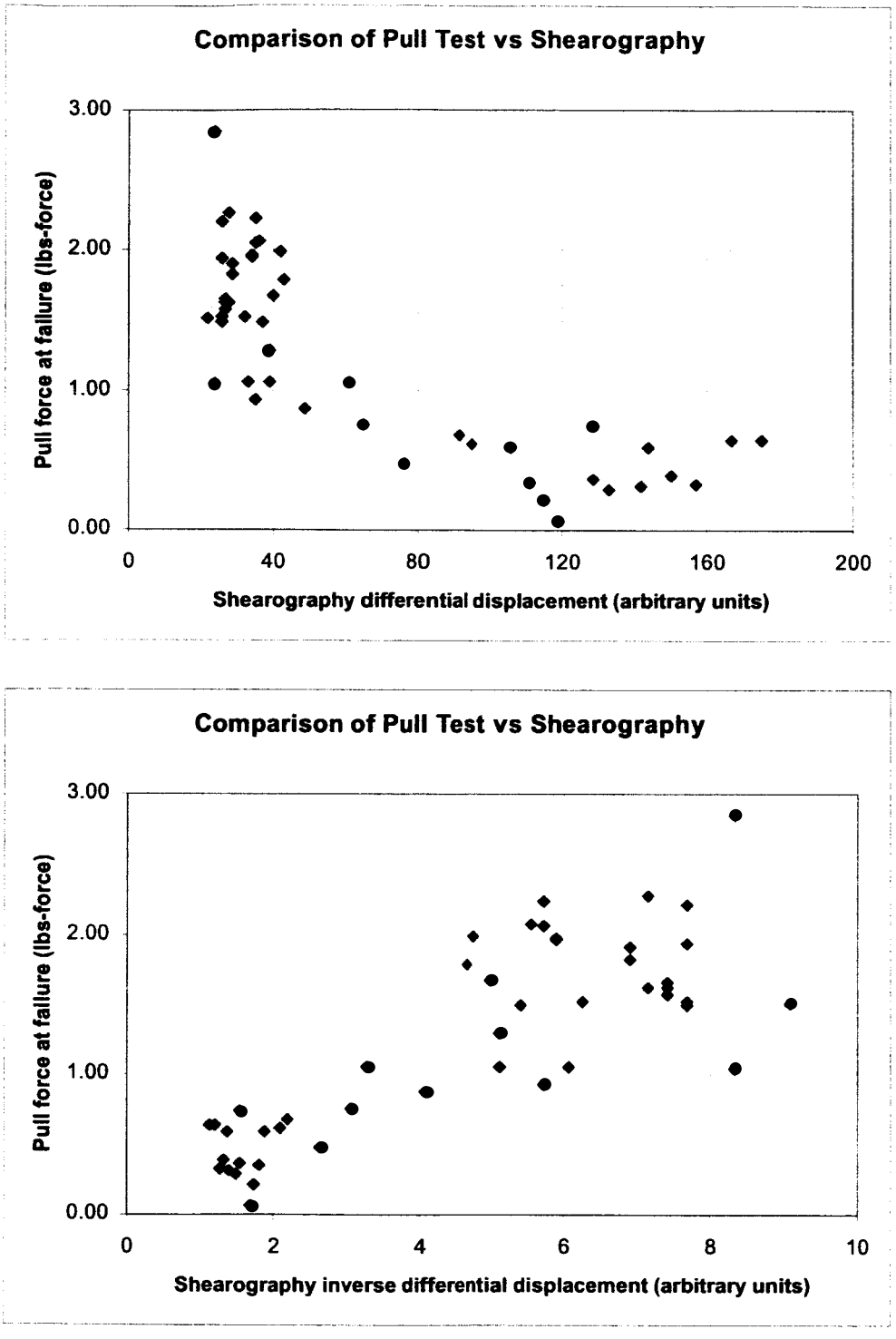

Figure 10. Pull test results compared to the shearography differential displacement results of Figure 9, averaged over the center of each tile. The bottom plot uses inverse differential displacement, which results in a roughly linear relationship with pull force.

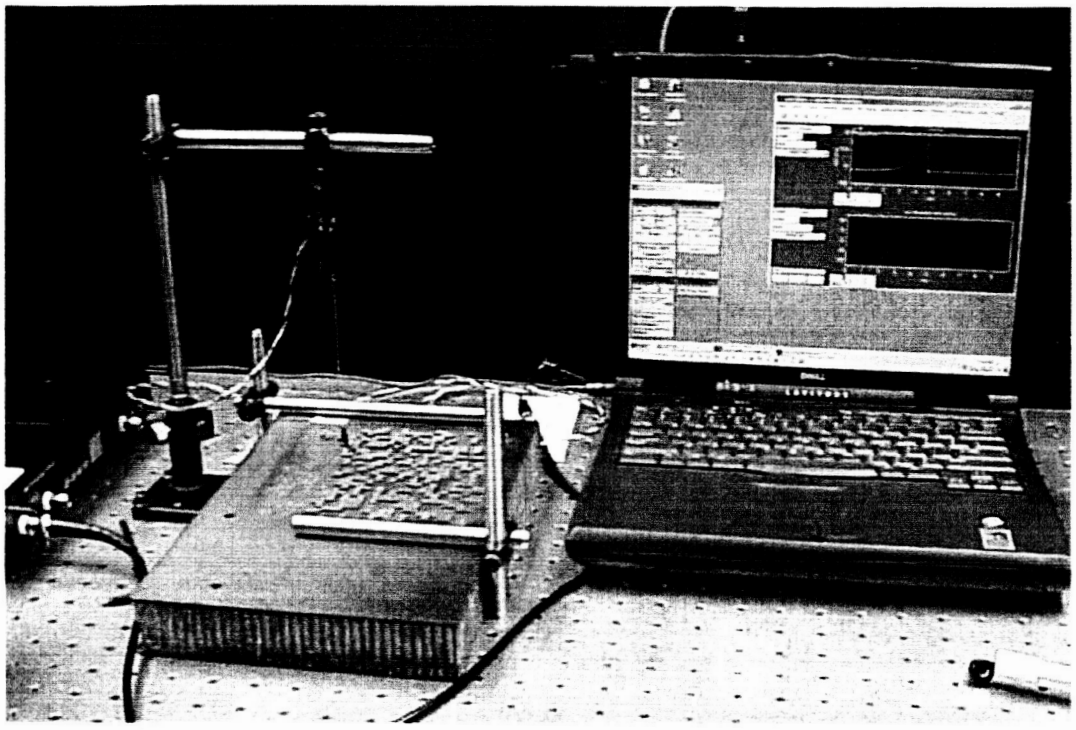

Figure 11. BAT Mask tile pull test set up.

4. Specular Surface Honeycomb Panel

As noted earlier, shearography has been demonstrated to give good results with diffuse surface honeycomb panels in identifying bonding failures between the core and skin. Vacuum, pressure, and thermal excitation have been used successfully. At the cell walls of the honeycomb core, where the skin is attached, the surface is constrained, and no change in slope can occur in response to the excitation. At the interior of the cells, however, the surface is free to respond and will appear different in the display of differential surface gradient. With a well bonded structure, the distinct honeycomb pattern of the core stands out in the display, and any bonding failure is readily apparent as an interruption of that pattern. In the present application, however, the primary challenge appeared to be that the panels have a specular surface and do not produce the speckle patterns needed for shearography. The approach we used was to generate the speckles by illuminating some other diffuse surface with laser light and then use the specular surface as a mirror to view them. In principle, this configuration should produce a display very similar to that obtained from a diffuse surface honeycomb panel.

The most appropriate excitation appears to be a slight pressure applied from inside the honeycomb core. The core has a system of holes that allow the pressure to equalize over the interior cells; however, all external holes must be sealed. A vacuum excitation from outside the panel was considered but appeared to be impractical because the specular

surface was not supposed to be touched and a special vacuum chamber would need to be constructed to fit the panel and seal at the edges. In addition, the sample panel was in rather poor condition and would have been difficult to seal up this way.

The experimental configuration is illustrated in Figure 12. The speckles are generated by expanding the laser beam and passing it through a ground glass diffuser. The diffuser is then imaged through the specular surface, using it as a mirror. Figure 13 shows the actual test set up. The laser light comes in from the left and passes through the microscope objective and pinhole at the left side of picture to the ground glass diffuser, which is seen as the green circle to the left of center. The honeycomb panel, which has portions of the specular aluminum coating stripped away, is mounted vertically at the back edge of the optical table. The image of the diffuser, reflected by the specular surface, is the bright green spot (right of center), and the interferometer and camera appear in front of the diffuser image.

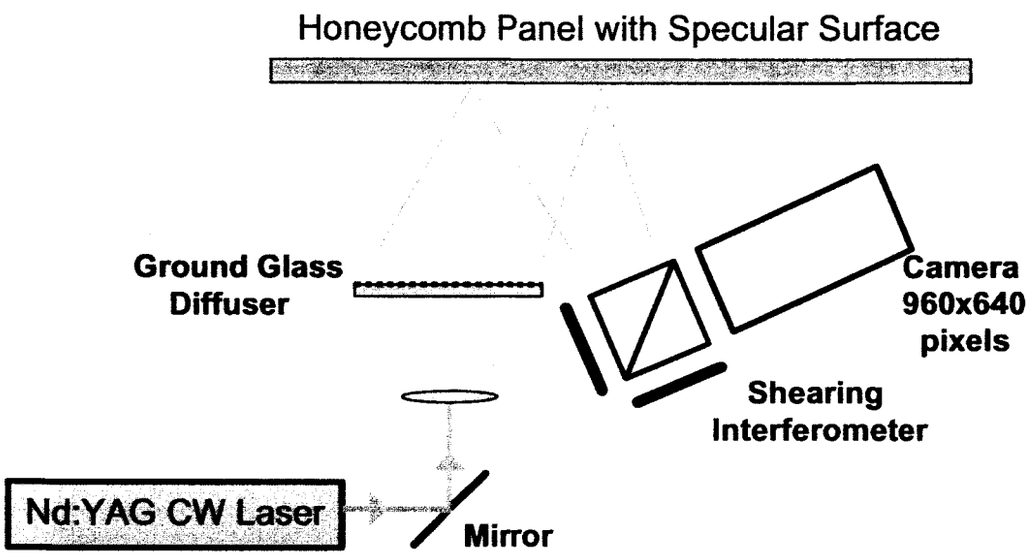

Figure 12. Specular surface honeycomb panel test configuration. The speckle is generated by passing the laser light through the ground glass diffuser and imaged using the specular surface as a mirror.

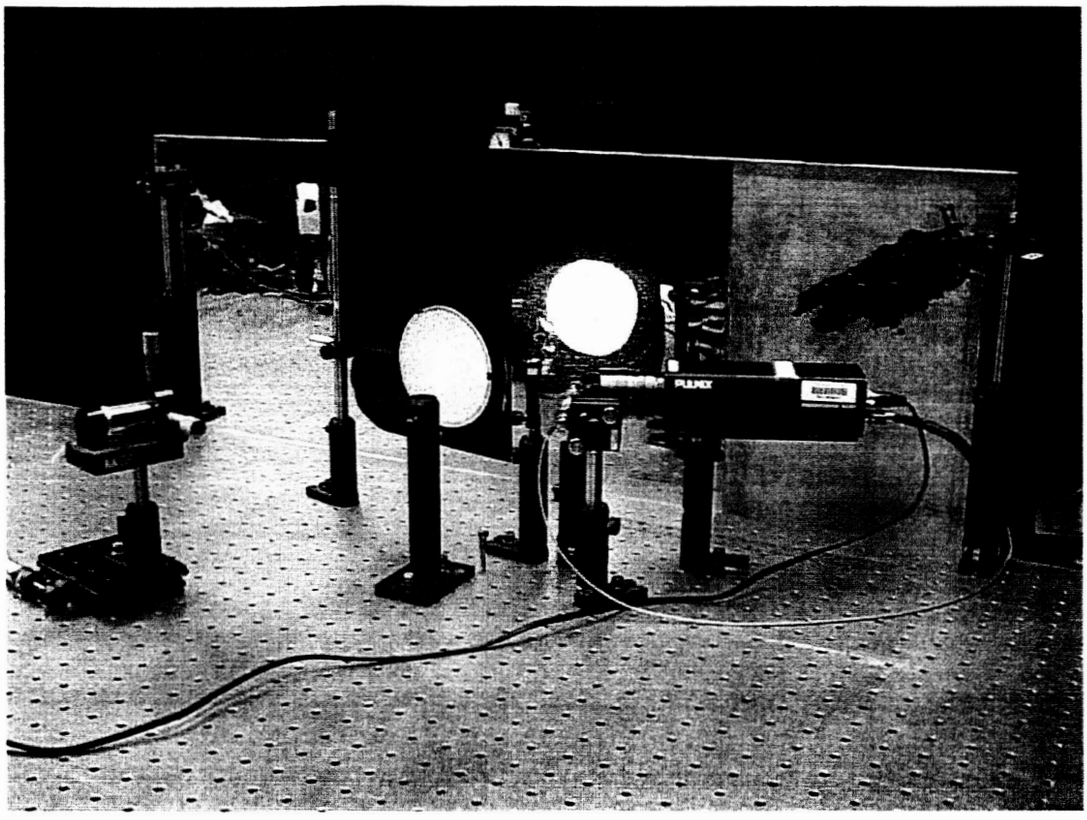

Figure 13. Specular surface honeycomb panel test set up. The laser light comes in from the left and passes through the microscope objective and pinhole (left side of picture) to the ground glass diffuser (green circle left of center). The honeycomb panel is mounted vertically at the back edge of the optical table, and the image of the diffuser, reflected by the specular surface, is the bright green spot (right of center), and the interferometer and camera appear in front of the diffuser image. Portions of the specular aluminum coating had been stripped away, revealing the fiberglass layer.

Ideally for nondestructive evaluation of these structures, it is desirable to have a positive verification that the structure is sound by identifying the characteristic honeycomb pattern in the differential displacement display. We were unable to obtain a good pattern; however, we were able to identify areas where large-scale bonding failures were readily apparent in the results. In Figure 14, for example, the speckle fringe pattern indicates an area, on the order of a couple inches, that is not bonded to the core.

The very small cell size of the core and possibly the composition of the skin might both contribute to the difficulties in imaging the honeycomb pattern. The skin on the panel consists of two layers, a fiberglass fabric bonded to the honeycomb core, covered by an aluminum sheet, which was polished to a mirror finish. The honeycomb cells were hexagonal, about 3 mm across. Although the shear distance can normally be adjusted the

scale size of the work piece, as the fringes become smaller they tend to get lost in the speckle noise. We observed this when the shear distance got down to 1 mm, which is on the order of half the cell size. In order to show that this was not related to the method of dealing with the specular surface, we use a standard shearography configuration to examine a portion of the panel where the specular layer had been stripped away, leaving the underlying fiberglass. The results were very similar to that obtained with the specular surface, indicating that the principle of imaging the speckles using it as a mirror is valid.

In order to get fringe resolution down to the cell size of the panel, the imaging configuration should be modified to increase the apparent cell size in the image. This is probably most easily done by using a longer focal length lens on the camera. While in a production environment it would be desirable to also increase the number of pixels in the camera, this is probably not necessary to prove the applicability of shearography. It should be pointed out that the double layer skin, particularly the stiffness of the aluminum layer combined with the small cell size, might also affect the ability to display a good pattern.

Figure 14. Specular honeycomb panel with bonding failure. The fringes indicate large scale areas where the skin is not bonded to the core. The lighter gray area below the fringe pattern is thought to be a region of good bonding.

Conclusions and Recommendations

In the evaluation of tile bonds on the BAT mask, the system was able to pretty clearly identify the tiles that were poorly bonded and appears to be quite effective for nondestructive evaluation in that application. For the full size mask, however, a fixture would need to be constructed to hold the mask while the vibration is applied. Since the mask is quite large, it is unlikely that inspection could be conveniently done in a single pass. It would be necessary to examine the mask in a sequence of spots, which would probably be most easily done by moving the mask rather than the inspection system. Because of the inherent robustness of shearography measurements, this should not be difficult. There is no need for the system to be set up on an optical bench; only the camera and interferometer would need to be mounted together on a small rigid plate.

The "spot size" (the area that can be examined at one time) could be scaled up fairly easily by using a more powerful laser, particularly a pulsed laser as described above, and/or by allowing the camera to integrate over a longer time period. A system intended specifically for large area vibration analysis should use a pulsed laser and eliminate the acousto-optic modulator, which would greatly increase the optical efficiency, with a corresponding increase in the spot size.

For the specular surface honeycomb panel, the technique of generating speckles with some other diffuse surface and imaging them through the mirror-like panel surface appears to be valid. This technique opens up the use of shearography to a new class of objects that could not have been examined using more traditional shearography configurations. The results obtained here are encouraging, but further development should be undertaken to demonstrate the general applicability of the technique and to establish a firm quantitative foundation.

Regarding the application of shearography to the nondestructive evaluation of this particular honeycomb, it has been demonstrated that large scale bonding failures can be identified with the system as configured. However, to reduce the scale size that can be evaluated to match the honeycomb core cell size, the optical configuration should be modified to increase the image size of the surface under test.

References

[1] G. Lu, B.A. Bard, and S. Wu, "A Real-time Portable Phase-stepping Shearography System for NDE," *Proc. Soc. Photo-Opt. Instrum. Eng.*, **3397-25**, 1998.

[2] B. A. Bard, "Laser-Modulated Phase-Stepping Digital Shearography for the Quantitative Analysis of Structural Vibration," Ph.D. Thesis, The Pennsylvania State University, August 1997.

[3] J. W. Goodman, "Statistical Properties of Laser Speckle Patterns," in J. C. Dainty, Ed., *Laser Speckle and Related Phenomena,* Springer-Verlag, 1984.